Higher-harmonic generation in boron-doped silicon from band carriers and bound-dopant photoionization

Fanqi Meng [1,*] Frederik Walla [1] Sergey Kovalev,[2] Jan-Christoph Deinert [2] Igor Ilyakov,[2] Min Chen,[2] Alexey Ponomaryov,[2] Sergey G. Pavlov [3] Heinz-Wilhelm Hübers [3,4] Nikolay V. Abrosimov [5] Christoph Jungemann [6,†] Hartmut G. Roskos [1,‡] and Mark D. Thomson [1,§]

[1]*Physikalisches Institut, J. W. Goethe-Universität, Max-von-Laue-Strasse 1, 60438 Frankfurt am Main, Germany*
[2]*Helmholtz-Zentrum Dresden-Rossendorf, Bautzner Landstrasse 400, 01328 Dresden, Germany*
[3]*Institute of Optical Sensor Systems, German Aerospace Center (DLR), 12489 Berlin, Germany*
[4]*Institut für Physik, Humboldt-Universität zu Berlin, 12489 Berlin, Germany*
[5]*Leibniz-Institut für Kristallzüchtung (IKZ), 12489 Berlin, Germany*
[6]*Institut für Theoretische Elektrotechnik, RWTH Aachen, 52062 Aachen, Germany*

(Received 20 December 2022; accepted 1 September 2023; published 9 November 2023)

We investigate ultrafast harmonic generation (HG) in Si:B, driven by intense pump pulses with fields reaching $\sim$100 kV cm^{-1} and a carrier frequency of 300 GHz, at 4 K and 300 K, both experimentally and theoretically. We report several findings concerning the nonlinear charge carrier dynamics in intense sub-THz fields: (i) Harmonics of order up to $n = 9$ are observed at room temperature, while at low temperature we can resolve harmonics reaching at least $n = 11$. The susceptibility per charge carrier at moderate field strength is as high as for charge carriers in graphene, considered to be one of the materials with the strongest sub-THz nonlinear response. (ii) For $T = 300$ K, where the charge carriers bound to acceptors are fully thermally ionized into the valence subbands, the susceptibility values decrease with increasing field strength. Simulations incorporating multi-valence-band Monte Carlo and finite-difference-time-domain (FDTD) propagation show that here, the HG process becomes increasingly dominated by energy-dependent scattering rates over the contribution from band nonparabolicity, due to the onset of optical-phonon emission, which ultimately leads to the saturation at high fields. (iii) At $T = 4$ K, where the majority of charges are bound to acceptors, we observe a drastic rise of the HG yields for internal pump fields of $\sim$30 kV cm^{-1}, as one reaches the threshold for tunnel ionization. We disentangle the HG nonlinear response into contributions associated with the initial photoionization and subsequent motion in the bands, and show that intracycle scattering seriously degrades any contribution to HG emission from coherent recollision of the holes with their parent ions.

DOI: 10.1103/PhysRevResearch.5.043141

I. INTRODUCTION

The future of semiconductor electronic devices relies on continuing to test and refine the physical description of carrier dynamics for increasingly shorter time scales and higher electric field strengths (i.e., sub-picosecond times and approaching the MV cm^{-1}range). Experiments with ultrashort, high-field pulses, in particular observing nonlinear higher order harmonic generation (HG) [1–5], provide a sensitive probe into the carrier response, as these nonlinear currents are dictated by the precise carrier distribution and scattering processes, band structure, interactions between band carriers and dopant/impurity ions, and, at low temperatures (where charges are bound to acceptors), field-driven ionization.

In the journey of HG from free carriers in semiconductors, pioneering studies using mid- [6] and far-infrared [7,8] pulses from molecular lasers were generally restricted to $\sim$nanosecond pulses. Although the estimated peak electric field reached over $\sim$100 kVcm^{-1}, no harmonics higher than third order were reported, and the sub-picosecond dynamics were not resolved. Nevertheless, they fueled the development of theoretical descriptions, including the role of band nonparabolicity and carrier relaxation [9,10]. The availability of high-field (sub-)picosecond THz pulses (e.g., from free-electron lasers or femtosecond-amplifier-laser sources) allows one to finally reach the nonperturbative field regime on the native time scales for the carrier dynamics [1,5]. Besides fundamental interest, the HG process can be considered for practical use for frequency conversion or frequency comb generation, and the efficiency can be enhanced, e.g., using resonant cavities [11].

In this paper, we investigate HG in weakly p-doped bulk silicon in a focused 0.3-THz radiation field reaching maxi-

*f.meng@physik.uni-frankfurt.de
†cj@ithe.rwth-aachen.de
‡roskos@physik.uni-frankfurt.de
§thomson@physik.uni-frankfurt.de

mum incident peak fields of ∼100 kV cm^{-1} (all field values here and in the following specify the field strength in vacuum, as the field strength within the specimens varies locally due to the formation of standing waves). In contrast to our previous study at lower fields (and higher frequencies) [1,11], these fields are strong enough to induce tunnel ionization of the impurity atoms at low temperature, and to drive band carriers out in k space to sufficiently high kinetic energies to reach the threshold $\mathcal{E}_{op}$ for scattering by optical-phonon emission (where $\mathcal{E}_{op} = 63.3$ meV at the Γ point for both TO and LO phonons [12]).

These results are complemented with large-scale time-dependent Monte Carlo (MC) simulations, addressing both (i) the local microscopic physics, to elucidate how the lh/hh carrier distributions, band anharmonicites, scattering rates (and photoionization of bound dopants at low T) contribute to the harmonic generation process, and (ii) propagation effects, by incorporating the MC simulations into a FDTD scheme.

II. EXPERIMENTAL

The experiments were conducted at the HZDR (Dresden) by employing the TELBE superradiant undulator source, where we used linearly polarized THz pulses tuned to a carrier frequency of $\nu_1 = 300$ GHz, with a pulse duration of $T_1 = 14.1$ ps (FWHM) and pulse energies up to 1 μJ at a 50-kHz repetition rate. We performed two series of experiments with two Si:B samples: (i) at $T = 300$ K (Sample A: $N_d = 5.75 \times 10^{15}$ cm^{-3}, thickness $L = 900$ μm) where the dopant acceptors are fully ionized and one measures the nonlinear response of a constant population of band holes, and (ii) at $T = 4$ K (Sample B: $N_d = 5.0 \times 10^{16}$ cm^{-3}, thickness $L = 272$ μm) where essentially all holes are bound to their parent ions and are photoionized into the valence bands during the pump pulse. The higher dopant concentration (Sample B) was used for the low-temperature experiments to achieve stronger harmonic emission signals, which were close to the noise floor for Sample A at $T = 4$ K. Preceding the sample, we employed a low-pass filter to suppress residual harmonics from the source, followed by two polarizers [2] to allow continuous variation of the strength of the pump field in the sample. Following the sample, a calibrated high-pass filter [1] was used to reduce the amplitude of the fundamental to allow a more balanced signal level for the overtones. The emitted field from the sample was reimaged into an electro-optic (EO) crystal for coherent time-domain detection. Incident and detected on-axis temporal field strengths were determined by calibrating the reference signal with the fluence determined from an additional measurement of the pump beam profile. Details of the samples and determination of doping concentration, field calibration, and spectral correction for the filters and EO response are given in the Appendix.

III. RESULTS

A. Overview of the findings

Figure 1 shows conceptual aspects of the experiments performed at 300 K [Fig. 1(a)] and 4 K [Fig. 1(b)] together with spectra recorded at the two temperatures at the maximal field strength available in the experiments [Fig. 1(c)].

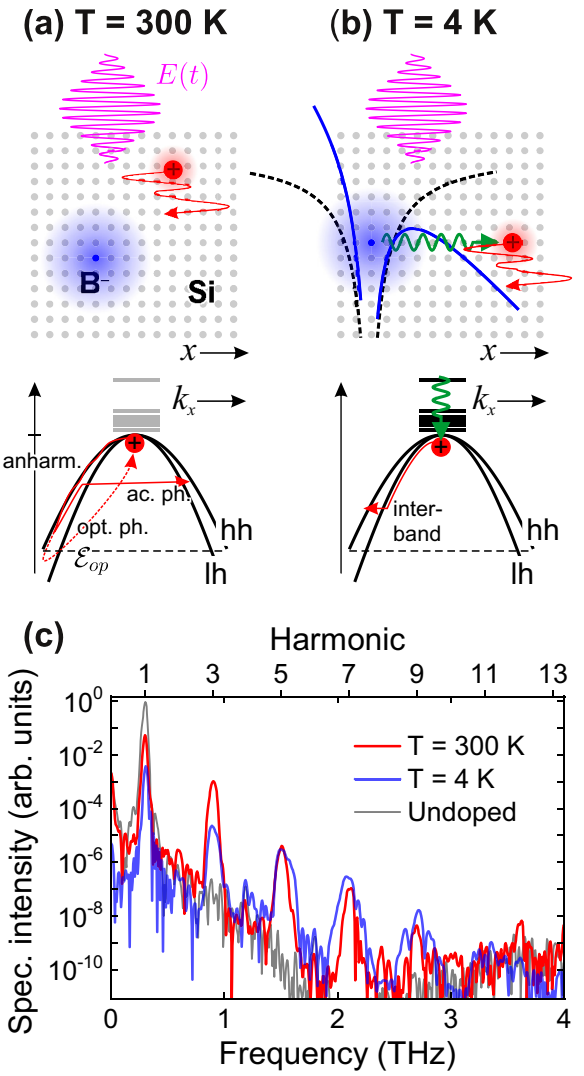

FIG. 1. Overview of strong-field harmonic generation in Si:B at (a) $T = 300$ K—band motion with thermally ionized holes including both band nonparabolicity and energy-dependent scattering; (b) $T = 4$ K, whereby light holes are first generated by tunnel ionization of acceptors, followed by significant lh → hh scattering (amplitude of hole trajectories not to scale). (c) Examples of experimental emission intensity spectra for optimal available conditions at $T = 300$ K and $T = 4$ K (measured at the maximum achievable fields with samples A and B, respectively—see text). Relative spectral intensities scaled to aid visual comparison. Note that absolute/optimal HG yields vs T depend on a complex interplay between pump-field strength, dopant density, sample thickness, and the resulting Drude absorption and standing-wave effects for the pump pulse, as addressed in Secs. III B and III C. Linear transmitted fundamental spectrum with undoped sample included for comparison.

At room temperature, the impurities are ionized and one observes the signatures of the nonlinear response of the charge carriers accelerating and scattering in the incident THz field (linearly polarized in x direction, propagating in z direction). As indicated in the lower panel of Fig. 1(a), the nonlinear response is determined by the nonparabolicity of the heavy- and light-hole valence bands and by the *relaxational nonlinearity* associated with the absorption and emission of acoustic and

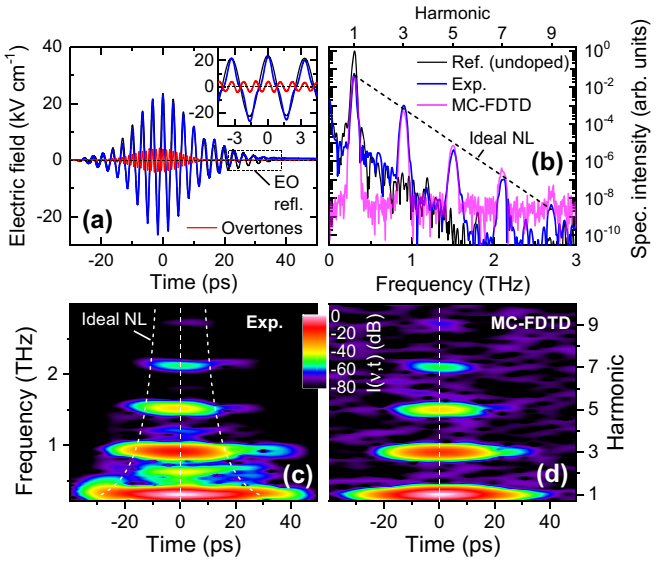

FIG. 2. (a) Experimental transmitted temporal field for a Si:B sample (Sample A: $N_d = 5.75 \times 10^{15}$ cm^{-3}, $T = 300$ K) for an incident pump peak field of $E_0 = 115$ kV cm^{-1} (blue curve), as well as the field of the overtones without fundamental (red) and scaled reference data for an undoped sample (black). Inset shows detail around the pulse peak. (b) Corresponding intensity spectra, as well as spectrum from MC-FDTD simulations with $E_0 = 100$ kV cm^{-1} (see text for discussion of pump field scaling between theory and experiment). (c) Experimental and (d) MC-FDTD spectrograms (common color scale as shown). Included in (b) and (c) are dashed curves for the relative intensity and duration, respectively, for ideal nonlinear HG (for the latter, assuming a Gaussian pulse profile, such that $T_n \sim T_1/\sqrt{n}$, curves shown for $T_n = \pm 2T_{\mathrm{FWHM}}$).

optical phonons, which gives rise to HG due to the energy dependence of the scattering rates. As presented below, we can distinguish these two contributions in the MC simulations by analyzing the spectra of both the time-dependent ensemble-averaged current [proportional to the group velocity $v(t)$] and wavevector $k(t)$, the latter essentially independent of the band nonparabolicities. Charged impurity scattering turns out not to play a strong role for the nonlinear response. At low T, most of the impurity atoms are initially in the neutral state. When they are exposed to a radiation field with rising field amplitude, one observes an increase of the nonlinear susceptibility $\chi^{(n)}$, which originates from the growth of the number of free holes by impact ionization and—setting in at fields of $\sim$30 kV cm^{-1}—by additional tunnel ionization, as indicated in Fig. 1(b). The tunneling process mainly populates the light-hole states from which scattering rapidly redistributes the holes in the valence band. We show that near the ionization threshold, a significant HG contribution is due to these "generational" nonlinear currents, while for higher pump fields the subsequent band nonlinearities dominate.

B. Room-temperature harmonic generation

We begin with the detailed description of the results measured at $T = 300$ K, to study the nonlinear response of a constant density of thermally ionized band holes. Examples of the fields measured behind the sample are shown in Fig. 2(a) for an incident peak pump field of $E_0 = 115$ kV cm^{-1}, with the corresponding intensity spectrum and spectrogram in (b) and (c), respectively [the spectrogram calculated with a temporal gate $w(t) = e^{-2t^2/T_g^2}$ with $T_g = 10$ ps]. Here, the odd overtones from $n = 3$ to 9 are clearly resolved. As shown in Fig. 2(b), the relative spectral intensity vs harmonic n is quite close to that expected for an ideal nonlinear HG process ($I_n \sim a^{-n}$, dashed curve), as is the progressive reduction in pulse duration T_n for each harmonic in Fig. 2(c), where some deviations are expected due to saturation/propagation effects discussed below. Note that as we consider lower-order harmonics, the overtone emission does not manifest as subcycle bursts in the time domain [13], but rather follows the intensity envelope of the pump pulse.

We note that in Figs. 2(b) and 2(c), one can resolve finite signals about the *even* harmonics ($n = 2, 4$) about $t = 0$ (also observed at low temperature in the next section). While the inversion symmetry of the medium should forbid the generation of these harmonics in the bulk (for a many-cycle pulse), they likely arise due to residual surface harmonic generation [14] due to a slight beam angle/asymmetry (this supported by the fact that their strengths were not repeatable in different measurements).

The theoretical modeling of the HG emission is based on Monte Carlo (MC) simulations of an ensemble of holes in the time-dependent field. The simulations include the dynamics of the heavy-hole (hh), light-hole (lh), and split-off (so) valence bands, realistic 3D band structures, and acoustic-/optical-phonon scattering (as well as charged impurity scattering, when expected to contribute significantly), similar to the treatment employed previously in the context of high-frequency Si devices [15,16]. As significant propagation effects also occur, including standing-wave effects for the pump field [1], one must go beyond a description of the local response to describe the experimental results. Hence we embedded the MC simulations in a 1D (plane-wave) finite-difference time-domain (FDTD) propagation scheme with a full, self-consistent approach for the charges/fields for the simulations at high fields (as opposed to an earlier perturbative approach [17], see also [18]), typically with a step size of $\delta z = 1$ μm along the propagation direction. To investigate the microscopic HG mechanisms, local MC simulations were performed, i.e., at a single internal z point in the bulk, as in our previous report [1].

An example of the emitted spectrum/spectrogram from such MC-FDTD simulations is shown in Figs. 2(b) and 2(d), respectively, and shows very good agreement with the experimental data. Note that the noise floor of the MC-FDTD results is due to the statistical fluctuations for the ensemble, which was restricted to $\leqslant 10^7$ holes in order to achieve practical calculation times. As discussed below, these results contain both local-saturation and propagation effects, involving changes in the carrier distribution and scattering dynamics during the pump pulse.

The dependence of the amplitudes of the transmitted harmonic fields on that of the incident pump field is shown in Fig. 3(a), for both experimental and MC-FDTD results. The data are obtained via band-pass filtering the spectral fields about each $\omega_n = 2\pi\nu_n$ and extracting the peak temporal field after transforming each back to the time-domain (see

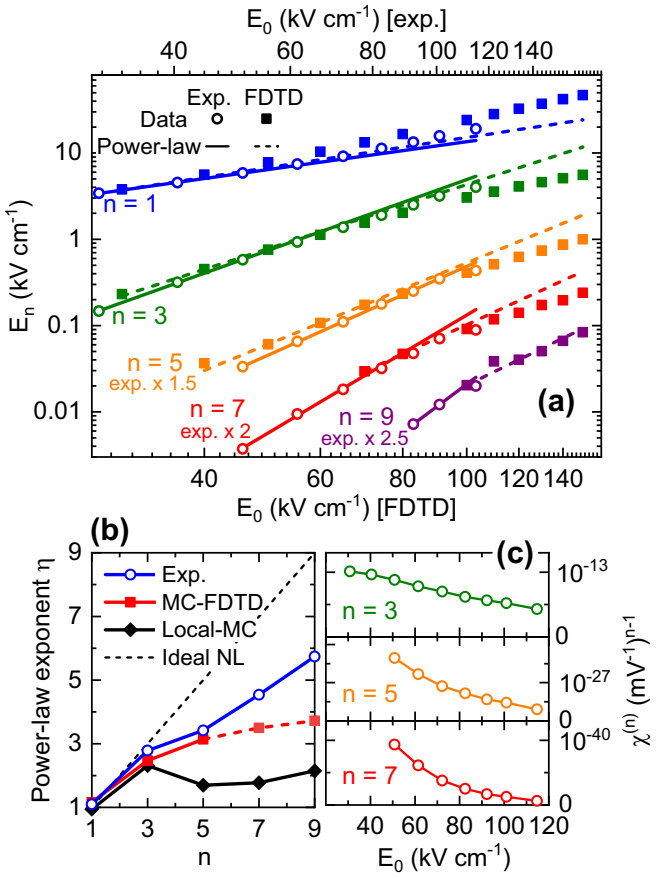

FIG. 3. (a) Pump field dependence of transmitted harmonic peak fields (Sample A: $N_d = 5.75 \times 10^{15}$ cm^{-3}, $T = 300$ K, $L = 900$ μm). Experimental results (open circles), and MC-FDTD results (filled squares) vs peak pump field (E_0, incident external to the sample) for each odd harmonic $n = 1$–9. Respective power-law fit to low-field ranges included as straight lines. To aid visual comparison, experimental and MC-FDTD plotted vs different horizontal axis (bottom: experimental data; top: MC-FDTD data with a scaling factor of 0.9), while experimental higher-harmonic fields ($n = 5, 7, 9$) are scaled by the factors given in the labels. (b) Power-law exponents from (a) vs n, from experimental and MC-FDTD data, as well as single-point (bulk) MC simulations. Note that the resolvable range of experimental data for $n = 7, 9$ are already well in the saturation regime. (c) Nonlinear susceptibilities $\chi^{(n)}$ calculated from experimental peak fields in (a) after correction for Drude absorption (see main text)

Appendix for temporal waveforms vs n). In terms of a quantitative comparison between theory and experiment, while we endeavoured to calibrate the experimental pump and detected harmonic fields as accurately as possible, some systematic errors may arise, e.g., due to residual frequency-dependent imaging of the axial fields exiting the sample to the EO-detection focus. Hence, to aid comparison of the trends (in particular, the low-field growth and subsequent saturation), in Fig. 3(a) we plot the respective results with a small rescaling of the relative pump fields (the bottom x axis is for the experimental data, and the top x-axis data is for simulation, which is scaled by a factor of 0.9), and apply modest correction factors to the field values E_n for $n = 5, 7, 9$ (as indicated in the labels). A comparison of the unscaled experimental and simulated results is included in the Appendix. Given the experimental error margin for the field calibration, the agreement is seen to be very reasonable, especially as no scaling is applied to $E_{1,3}$. Also included are power-law fits $E_n \sim E_0^{\eta_n}$ using the lowest available field ranges in each case; the exponent η_n is plotted in Fig. 3(b). Several key aspects are evident: Firstly, one sees with increasing field that the transmitted fundamental wave ($n = 1$) grows superlinearly, in both the experimental and MC-FDTD data. As discussed further below, this is due to the increase of the scattering rate of the holes at higher fields, which causes a reduction of the Drude absorption at ν_1, and amounts to a bleach factor of ~2 at the highest field (the linear Drude absorption depth of the sample at ν_1 is 230 μm). For $n = 3$, one observes an initial growth close to the ideal power-law exponent of $\eta_3 = 3$, although the data visibly *saturate* by a factor ~2 at the highest fields, despite the bleach of the fundamental pump field. A similar saturation is observed for $n = 5, 7, 9$ (note that the noise levels in the MC-FDTD preclude fitting the data for $n = 9$ at sufficiently low fields to avoid saturation). These nonideal field dependencies are due to an interplay between local (microscopic) saturation and propagation effects, and will be disentangled below with the aid of local MC simulations. On the basis of the experimental fields, one can estimate an effective nonlinear susceptibility $\chi^{(n)}$ for each harmonic, the results of which are shown in Fig. 3(c) for $n = 3, 5, 7$. These are calculated following standard approaches [2] for unidirectional propagation (neglecting absorption and phase-matching), which yields,

$$E_n = \beta_n \chi^{(n)} E_1^n, \quad \beta_n = i\omega_n L/(2^n n_r c) A_n \tag{1}$$

with n_r the refractive index and c the vacuum speed of light. Due to the significant Drude absorption for both the pump and harmonics (which would lead to a underestimate of $\chi^{(n)}$ from the data), we include the factors $A_n = (1 - e^{-a_n L}/a_n L) e^{-\alpha_n L/2}$ [$a_n = (n\alpha_1 - \alpha_n)/2$] where α_n is the intensity absorption coefficient for each harmonic (the experimental bleach factor is also included to correct α_1 to avoid overestimating $\chi^{(n)}$, but only leads to a small correction, see Appendix). Clearly, the saturation effects with increasing E_0 lead to a reduction in the extracted values. For the lowest fields, we have $\chi^{(3)} = 1.0 \times 10^{-13}$ m^2 V^{-2}, which is highly consistent with the value $\chi^{(3)} = 0.9 \times 10^{-13}$ m^2 V^{-2} one can deduce from previous reports for Si:B with nanosecond pulses at $\nu_1 = 610$ GHz [7] for this dopant density.

It is instructive to compare these nonlinear susceptibilities to those of *bound* dopants at low T (for fields below the threshold for photoionization, in contrast to the next section), as previously reported by others for 3HG [5,19]. For the case of Si:P, while for low frequencies (where both ω and 3ω are off-resonant with respect to the transitions between bound states) the concentration-normalised value $\chi^{(3)}/N_d$ is significantly lower than for our band carriers here ($\chi^{(3)}/N_d = 1.7 \times 10^{-35}$ m^5 V^{-2}) by as much as three orders of magnitude [19]. However, as one approaches resonances (where $3\hbar\omega$ corresponds to a bound-state transition energy), it exhibits sharp peaks with values exceeding ours by more than an order of magnitude [5]. While this enhanced response is compelling, such bound-state resonances suffer from

being only accessible for very specific pump THz frequencies ($\gtrsim$2 THz), and the reabsorption of the 3HG signal wave is very strong. In comparison, the use of band carriers has the advantages of broadband, room-temperature applicability, where the (Drude) reabsorption actually falls off at the HG signal frequencies.

We note that besides the pump field dependence of the emission field strength, we also extracted the relative phases of the fields. As described in the Appendix, these vary by a small fraction of the fundamental cycle ($<0.2\pi$) while the trends vs E_0 are also reasonably well reproduced in the MC-FDTD results. A comparison with the local-MC response shows these trends comprise both contributions from the local intracycle phase as well as a dominant contribution from the accumulated phase shifts due to propagation.

In Fig. 4, we plot a selection of results from local (single z point) MC simulations vs field, where we stored and analyzed the time-dependent, ensemble-averaged band velocities $v_b(t)$ ($b =$ hh, lh, so) and occupation-weighted total velocity $v(t)$, wavevectors $k_{bj}(t)$ and their rms spreads $\sigma_{bj}(t)$ ($j = x, y, z$, where the pump field is polarized along the x direction), band populations $N_b(t)$, and scattering rates $\Gamma_b(t)$. As the so-band has only a very minor contribution, it was omitted in the following analyses. In Fig. 4(a), we plot the relative emission intensities V_n for each harmonic n, obtained by integrating the spectral intensity of $V(\omega) = |\mathcal{F}\{v(t)\}|^2$ about each ω_n. Also included are the fluences $F_n \propto |E_n|^2$ from the MC-FDTD results in Fig. 3(a) (scaled for comparison by a common constant for all n), which in the absence of any propagation effects would coincide with V_n for $n > 1$. One observes saturation in the local response with increasing field for all overtones as well as the fundamental. For the latter, its origin is clearly demonstrated in Fig. 4(b), where we plot $v(t)$ for hh and lh with a scaled profile of the pump field $E(t)$. The inset displays three oscillation periods at the center of the pulse. One sees how $v(t)$ undergoes strong clipping at each peak of $E(t)$, which is due to a rapid rise in momentum scattering, discussed further below. Integrated along the beam path, the decrease in local emission intensity is, however, overcompensated by reduced loss as shown by the blue lines (full and dotted) in Fig. 4(a). The loss reduction is also a consequence of the increase in scattering rate for the local current, which manifests as a weaker Drude absorption at ω_1 during propagation, and leads to the bleach effect seen in Fig. 3(a). Comparing the local and FDTD results in Fig. 4(a) allows one to draw additional conclusions concerning the role of propagation for the harmonics $n > 1$: The local saturation in the emission intensity for $n = 3$ is compensated by the bleach of the Drude absorption during propagation, weakening the saturation effect for the transmitted signal. This effect is also present to a lesser degree for $n = 5$, but is essentially absent for $n = 7, 9$, as here the increased scattering rate no longer causes a significant bleach of the Drude absorption. Moreover, with increasing n, the effects of a finite phase mismatch $\Delta k_n \sim \omega_n(n_{rn} - n_{r1})/c$ should also lead to additional saturation effects during propagation. In Fig. 4(c), we compare the relative contributions to the total emission intensity from hh and lh for each n. As expected, the linear response ($n = 1$) is dominated by hh, due to their much higher occupation, $N_{\rm hh}/N_0 \approx 0.85$ in thermal equilibrium, which does not vary

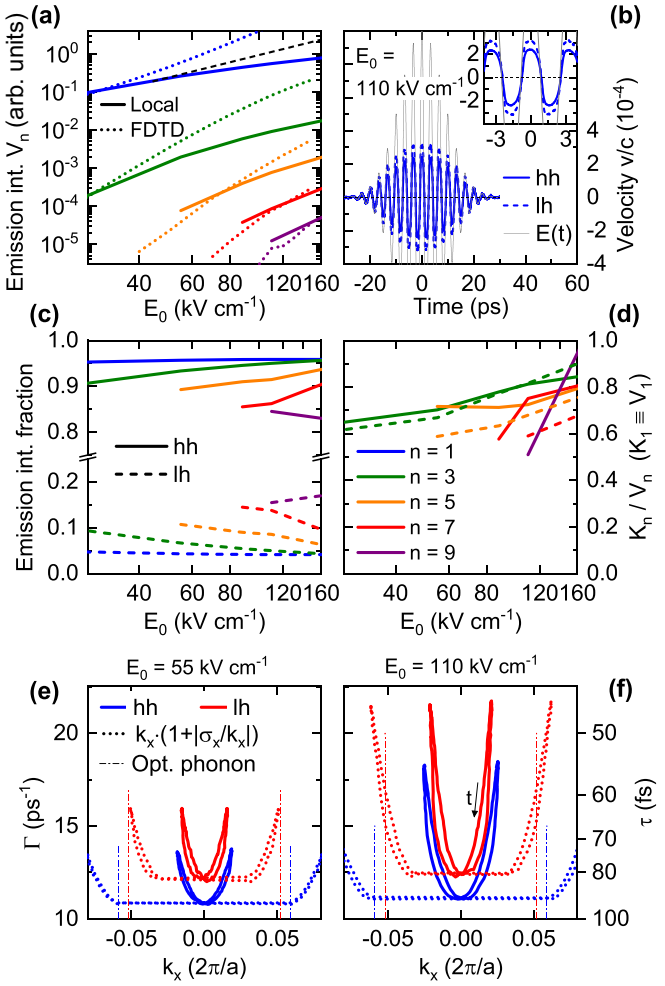

FIG. 4. Local MC results ($N_d = 5.75 \times 10^{15}$ cm^{-3}, $T = 300$ K). (a) Pump field dependence of relative emission intensities V_n for each odd harmonic $n = 1 - 9$ [solid curves, legend in (d)]. Scaled fluence from MC-FDTD (dotted curves) included for comparison [corresponding to data in Fig. 3(a)]. Black dashed curve corresponds to a linear dependence, for comparison with the curves for $n = 1$. Note that local internal pump fields used are $E_0' = \hat{t}_1 E_0$ (where $\hat{t}_1 = 0.46$ is the Fresnel field transmission entering the sample). (b) Time-domain (ensemble-average) velocity for $E_0 = 110$ kV cm^{-1} for both hh and lh, as well as scaled pump electric field profile $E(t)$. (c) Respective fraction of emission intensities from hh/lh for each n. (d) Ratio of nonlinear intensity due to $k_b(t)$ only (K_{bn}, see text) relative to emission intensity V_{bn}. [(e),(f)] Scattering rates $S(t)$ during the peak cycle of $E(t)$ for two peak pump fields ($E_0 = 55, 110$ kV cm^{-1}, respectively) plotted as loci vs the ensemble averages $k_{bx}(t)$. Also included are the same loci, but vs $k_{bx} \cdot (1 + |\sigma_{bx}/k_{bx}|)$ to reflect the extent of the high-energy tail of the distributions. Thresholds for opt. phonon emission for each band (corresponding to an energy of $\mathcal{E}_{op} = 63.3$ meV) included as vertical lines. Orientation of temporal hysteresis indicated by arrow in (f).

significantly during the pump excitation (in contrast to our previous simulations at $T = 10$ K [1] where $N_{\rm hh}$ rose to 0.93 in nonequilibrium, further depleting $N_{\rm lh}$). For the overtones, the relative contribution from lh increases with n, indicating that they have a stronger nonlinear response per hole than the hh (see below).

As mentioned in Sec. III A, one can distinguish two main mechanisms for the HG process: band nonparabolicity ("BNP") and energy-dependent scattering ("EDS"). To gauge their relative roles, we employ the same approach we used previously (Ref. [1], Fig. 4): One can obtain a quantity V_{bn} proportional to the emission intensity of each harmonic by integrating the spectral intensity $V_b(\omega) = |\mathcal{F}\{v_b(t)\}|^2$ of the ensemble-averaged group velocity $v_b(t)$ for each band b about each ω_n. Likewise, one can calculate the quantity K_{bn} from the spectral intensity $K_b(\omega) = |\mathcal{F}\{k_{bx}(t)\}|^2$ of the occupation-weighted wavevector component $k_{bx}(t)$, which describes the motion in k-space, rather than real space, and hence does not include the effect of BNP present in V_{bn}. In the case of ideal parabolic bands, the two quantities would be proportional. While BNP indeed has a finite influence on the precise scattering processes and hence $k_{bx}(t)$, the quantity K_{bn} still provides a reasonable measure for the nonlinear response in the hypothetical absence of BNP. By normalizing $K_{b1} \to V_{b1}$, for the overtones a ratio of $K_{bn}/V_{bn} \to 0$ or 1 corresponds to pure BNP or EDS, respectively. As shown in Fig. 4(d), the K_{bn}/V_{bn} values are all above 0.5 in the field ranges where harmonics can be extracted, increasing toward unity as the field amplitude increases. It indicates that, for the highest electric field used in our experiment, EDS dominates. One could also envisage that, at the electric field below 50 kV cm^{-1}, the BNP also plays an important role for certain higher order harmonics, i.e., $n = 7, 9$. This is in stark contrast to our earlier study [1] for $n = 3, 5$ at $T = 10$ K with $N_d \leqslant 10^{14}$ cm^{-3} and somewhat lower fields ($E_0' \lesssim 25$ kV cm^{-1}, $E_0 \lesssim 50$ kV cm^{-1}), where $K_{bn}/V_{bn} \ll 0.01$, and hence BNP heavily dominated the HG response. The major reason for this is that the higher fields in the present study allow to reach the threshold for optical-phonon emission (the TO/LO phonon being degenerate at the Γ point with $\mathcal{E}_{op} = 63.3$ meV [12]). This is not immediately obvious in Fig. 4(d) where K_{bn}/V_{bn} for $n = 3$ does not fall rapidly as the field strength decreases to $E_0 \lesssim 50$ kV cm^{-1}, the field range of our previous study [1]. This can be traced to the broadening effect by the higher value of T (300 K here, 10 K in [1]), whereby the broadened Fermi-Dirac distribution brings the more energetic carriers already close to $\mathcal{E}_{op}$ in thermal equilibrium before the pump excitation (the band filling at these densities N_d is still only a minor effect). This suppresses any sharp threshold behavior for K_{bn}/V_{bn} vs E_0 here, although experiments at somewhat lower T (but sufficiently high to maintain a thermally ionized hole population) should show a much clearer transition.

In Figs. 4(e) and 4(f) we plot the loci of the instantaneous, ensemble-averaged scattering rates $S(t)$ vs $k_{bx}(t)$ (for a cycle at the peak of the pump pulse) for peak pump fields $E_0 = 55$ and 110 kV cm^{-1}, respectively. To better reflect the magnitude of k_{bx} reached by the high-energy tail of the carrier distribution, we also plot the data vs $k_{bx}(t) \cdot (1 + |\sigma_x(t)/k_{bx}(t)|)$, i.e., $k_{bx}(t)$ extended by the instantaneous rms width $\sigma_x(t)$ of the distribution. Here one clearly sees that the k-space extent of the carrier distributions is significantly broader than the ensemble average. At $k_x = 0$, the hh distribution (unlike the lh distribution) already touches the threshold for LO/TO phonon emission, although the hh and lh scattering rates are still dominated by acoustic-phonon scattering. When driven out in k space, the hh and lh populations experience a strong increase of the scattering rate, much of which appears to be due to reaching and crossing the threshold for LO/TO phonon emission. At $E_0 = 110$ kV cm^{-1}, the increase in scattering is steeper for lh than hh. Moreover, a comparison of K_{bn} vs E_0 (not shown) also shows a higher ratio $K_{\mathrm{lh},n}/K_{\mathrm{lh},1}$ compared to $K_{\mathrm{hh},n}/K_{\mathrm{hh},1}$, i.e., the lh nonlinear response is dominantly from the higher EDS, and not a higher BNP. These effects arise due to the fact that the lh initially absorb more kinetic energy from the pump field, allowing the highest-energy lh to experience stronger optical-phonon emission before the lh → hh intracycle energy equilibration takes full effect.

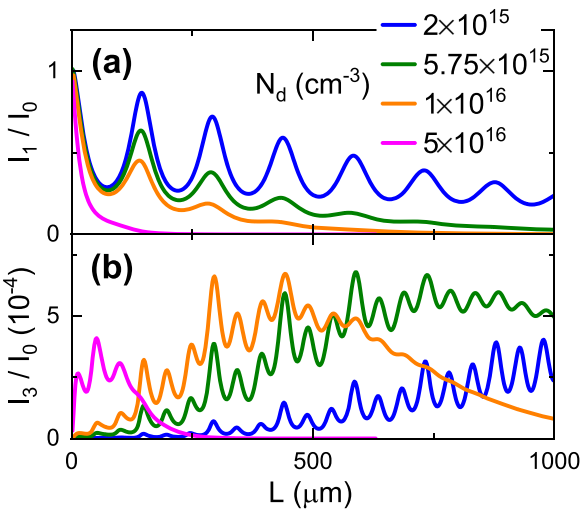

FIG. 5. Predicted transmitted (a) fundamental and (b) third-harmonic intensities $I_n(L)$ from FDTD simulations vs sample thickness L for selected dopant densities N_d ($T = 300$ K).

We now address how variations in the experimental parameters should affect the HG yield. For the role of dopant concentration N_d and sample thickness L, we performed a large set of FDTD simulations for selected N_d and vs dense set of L values. To achieve practical simulation times, instead of the full MC-FDTD used above, we employed an approximate approach where the velocity-field relation $v(E)$ is determined from local quasistatic MC simulations, and use this in the FDTD algorithm for each (N_d, L) combination. This approximate treatment still captures the interplay between nonlinear current density, Drude absorption, and standing-wave effects, and should be near-quantitative at least for $n = 3$. The results are shown in Fig. 5. For the fundamental wave [Fig. 5(a)], one sees how the increasing Drude absorption with N_d reduces the pump penetration depth (and suppresses the standing wave). This leads to the more complex dependence of the emitted third-harmonic intensity [Fig. 5(b)] on N_d and L. As could be expected, as N_d is increased, the optimal thickness L reduces. One also sees that for the highest doping concentration $N_d = 5 \times 10^{16}$ cm^{-3}, the maximum value of I_3 has begun to drop as the penalty from Drude absorption overwhelms the gain from a higher hole density. Hence, even for an optimally chosen sample thickness, the optimal value of dopant concentration is $N_d \sim 10^{16}$ cm^{-3}. Note that one also observes a more complex standing-wave interference structure for $I_3(L)$ vs L, which has both components from the fundamental wave and

third harmonic, demonstrating that multiple reflections in the sample for the latter are also important for the precise yield.

Concerning the dependence of the HG yields on pump frequency ω: For a given pump field amplitude, the excursion in k space during a field half-cycle is correspondingly smaller as one increases the frequency, going with ω^{-1} [18], which reduces both the nonlinear response due to nonparabolicity, and even more drastically, the energy-dependent scattering rate when falling below the threshold for optical-phonon emission. Given that scattering promotes the HG process, the reduction of scattering events during a shorter cycle (i.e., approaching a more ballistic regime) provides no benefit here.

To summarize this section, we find that in this pump field/frequency regime, the harmonic generation from band holes is dominated by energy-dependent scattering rates (especially due to reaching the threshold for optical-phonon emission), whose saturation from an ideal nonlinear response at high fields is due to the fact that once this threshold is reached, any subsequent excursion in k space is strongly suppressed. While this microscopic (local) effect dominates the pump field dependence, propagation effects must still be taken into account in order to quantitatively account for the experimental results.

C. Low-temperature harmonic generation

We turn now to the low-temperature case, where the vast majority of acceptors are in the neutral state and only a small residual density of holes reside in the valence bands before the pump pulse excitation. In our previous study of Si:B at low temperature [1], due to both the lower peak pump fields ($E_0 \lesssim 50$ kV cm^{-1}) and higher frequency ($\nu_1 = 1.29$ THz), we did not reach the threshold for significant tunnel ionization. Nevertheless, we could resolve both 3HG and 5HG in the emitted fields (measured only as intensity spectra obtained with far-infrared Fourier transform spectrometry), which arose from the residual band-hole density (which was seen to grow with increasing field due to carrier multiplication during the pump pulse, resulting in a moderately field-dependent value of $\chi^{(3,5)}$). Moreover, as mentioned above, the nonlinearity giving rise to the HG was found to be dominated by BNP, in particular as most holes did not reach the threshold energy for optical-phonon emission whereby EDS should become very strong.

Here at low temperature, we can reach peak external incident pump fields of $E_0 \sim 80$ kV cm^{-1} (and internal fields $E_0' \sim 40$ kV cm^{-1}), and more decisively at a significantly lower frequency of $\nu_1 = 0.3$ THz, such that the ponderomotive energy $U_{p,b} = q^2E_0^2/(4m_b\omega_1^2)$ [20] will be up to a factor ~50 higher ($U_{p,\mathrm{lh}} \sim 1.3$ eV for lh with $m_{\mathrm{lh}}/m_e = 0.15$), and the Keldysh parameter (an inverse measure of the onset of tunnel ionization for a required ionization energy I_p, where here $I_p = 45$ meV [12]) $\gamma_b = \sqrt{I_p/2U_{p,b}}$ also seven times higher ($\gamma_{\mathrm{lh}} \sim 0.13$, well into the tunnel regime). Note that we tentatively employ these expressions from the gas phase, where scattering (dephasing) is neglected and one assumes a ballistic trajectory for the ionized charges, as addressed below.

As per the results in Fig. 2 for $T = 300$ K in the last section, we first show a summary of the experimental emitted fields in Fig. 6 for the highest pump field $E_0 = 81$ kV cm^{-1}.

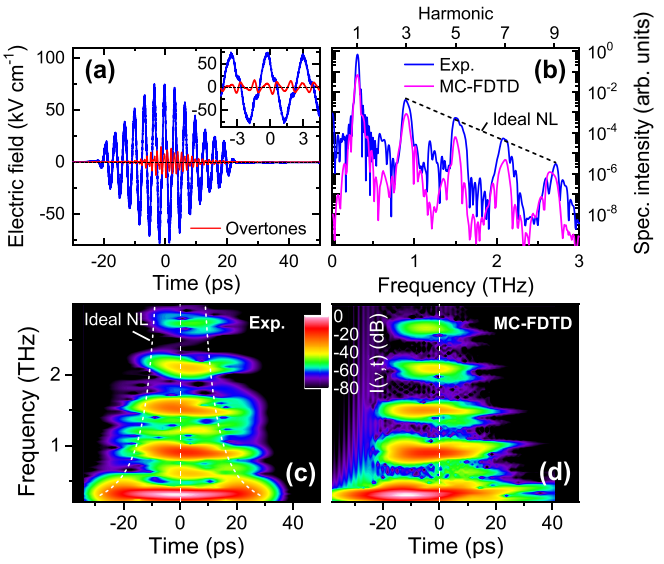

FIG. 6. (a) Experimental transmitted temporal field for Si:B sample (Sample B: $N_d = 5.0 \times 10^{16}$ cm^{-3}, $T = 4$ K) for an incident pump peak field of $E_0 = 81$ kV cm^{-1} (blue curve), as well as the field of the overtones without fundamental (red). Inset shows detail around the pulse peak. Note that a temporal window was applied to the wings of the pulse to suppress noise and reflections in the sample. (b) Corresponding intensity spectrum, as well as that from MC-FDTD simulations including tunnel ionization for $E_0 = 80$ kV cm^{-1} ($N_d = 5.9 \times 10^{16}$ cm^{-3}). Both spectra plotted with the same absolute intensity scale. (c) Experimental and (d) MC-FDTD spectrograms. Additional annotations per Fig. 2.

Compared to the results for $T = 300$ K, the intensity ratios between successive overtones are significantly smaller. The latter is also evident in the time-domain overtone field [Fig. 6(a), red curve], which shows a more complex interference of the $n = 3$ wave with those for $n > 3$. This we attribute to the inherently more nonlinear response for the present case, where photoionization must first occur (with a threshold in the time-domain for the pump pulse), as discussed further below. This is the main reason why one can readily resolve also the $n = 11$ harmonic in the spectra (where even an indication for the $n = 13$ harmonic is seen close to the noise floor—see Appendix). One also sees that the bandwidths of the overtones here are larger [see also Fig. 1(c)], increasingly so for higher n. These larger bandwidths could in principle indicate either successively shorter harmonic pulses (decreasing faster than the $T_n \sim T_1/\sqrt{n}$ rate for an ideal nonlinearity with a Gaussian pulse profile) or a frequency modulation of each HG field: An inspection of the experimental spectrogram [Fig. 6(c)] shows that the latter effect is significant, which we attribute to the fact that the hole populations vary during the pulse due to the tunnel ionization (addressed further below), and the wave mixing is more complex than just a multiphoton convolution of the components of the pump pulse spectrum, with both pump and overtone fields interacting with a time-dependent hole population. That the broadening is mostly due to local effects (rather than nonlinear refraction during propagation) is confirmed by comparing the spectra from FDTD-MC and local-MC simulations (presented below), the latter also showing such increased spectral widths.

As in Sec. III B, we performed MC simulations of the HG experiments. This required extending the MC scheme to incorporate the tunnel ionization process injecting holes into the bands, with a time-dependent density $N_b(t)$. To calculate the ionization rate $\partial_t N_b(t)$, we employed the ionization probability rates $w_{i,b}(E)$ established in the literature for a static electric field [21,22] and integrate $\partial_t N_b = w_{i,b}(t)(N_d - N)$ $(N = \Sigma_b N_b)$ during each time step with the field $E(t)$. The use of a static-field model for the instantaneous tunnel ionization rate has been shown to hold reasonably well in the context of ionization of gas atoms/molecules, at least in the strong-field regime ($\gamma \ll 1$) [23–25]. As asserted in [22], the tunneling vs field should be dominated by ionization into the lh band, which seems reasonable due to the $U_{p,b} \propto 1/m_b$ dependence for the ponderomotive energy. As a simplified approach, we then take $w_{i,\mathrm{hh}} \to 0$ and inject holes only into the lh band, which then can rapidly scatter into the hh band, as modeled by the MC treatment. Details of the ionization rate [formula, parameters for Si:B and plot of $w_{i,\mathrm{lh}}(E)$] are given in the Appendix.

The corresponding intensity spectrum and spectrogram from MC-FDTD calculations for conditions close to the experimental ones are shown in Figs. 6(b) and 6(d), respectively. The simulated results do exhibit a reasonable qualitative correspondence to the experimental data, although certain systematic deviations are present, as discussed below.

In Fig. 7, we present both the experimental and MC-FDTD simulation results for the pump field dependence of the HG emission. As the broadband EO field detection was only sensitive enough to resolve the harmonics for $E_0 \gtrsim 40$ kV cm^{-1}, we augmented the measurements of the 3HG-emission with a more sensitive low-bandwidth EO sensor for pump fields down to $E_0 \sim 10$ kV cm^{-1}, as shown. As significant distortions are seen in the envelopes of the filtered time-domain harmonics (see Appendix), we choose here to plot the results in terms of the emitted fluence $[F_n = \epsilon_0 c \int dt E_n^2(t)]$ to avoid any artifacts. One sees that at low-pump fields, the 3HG emission closely follows a power-law dependence, $F_n \propto E_0^{2\eta_3}$ with $\eta_3 = 3.54$. This behavior is comparable to that seen in our previous study at $T = 10$ K (with the same B dopant concentration as here) [1], where a value of $\eta_3 = 4.2$ was determined, which exceeds the value $\eta_3 = 3$ (for an ideal nonlinear process in a static medium) due to field-driven multiplication [26] of the residual band carriers (density N_r) during the pump pulse. The different value of $\eta_3 = 3.54$ here can be attributed to the different pump frequency. In [1,11], we employed the impact ionization model from [26] in its high-field limit, where the carrier multiplication factor $f = \Delta N/N_r \sim 1 - E_m^2/E^2$, with the characteristic field constant E_m increasing with ω_1. Hence $\partial_E f \sim +2E_m^2/E^3$, which should be larger for the previous experiments with $\nu_1 = 1.29$ THz and hence produce a larger value of η_3, which is at least qualitatively consistent with the two results. We can compare the observed 3HG fluence levels with those expected for *bound* dopants, by solving Eq. (1) with the dopant concentration and thickness of Sample B (neglecting standing wave effects). Here we use the low-frequency value of $\chi^{(3)}/N_d \sim 3 \times 10^{-38}$ m^5 V^{-2} calculated for Si:P [19], which should provide an upper bound for Si:B given that the latter has somewhat weaker bound-transition band strengths [27]. This result is also included in Fig. 7(a)

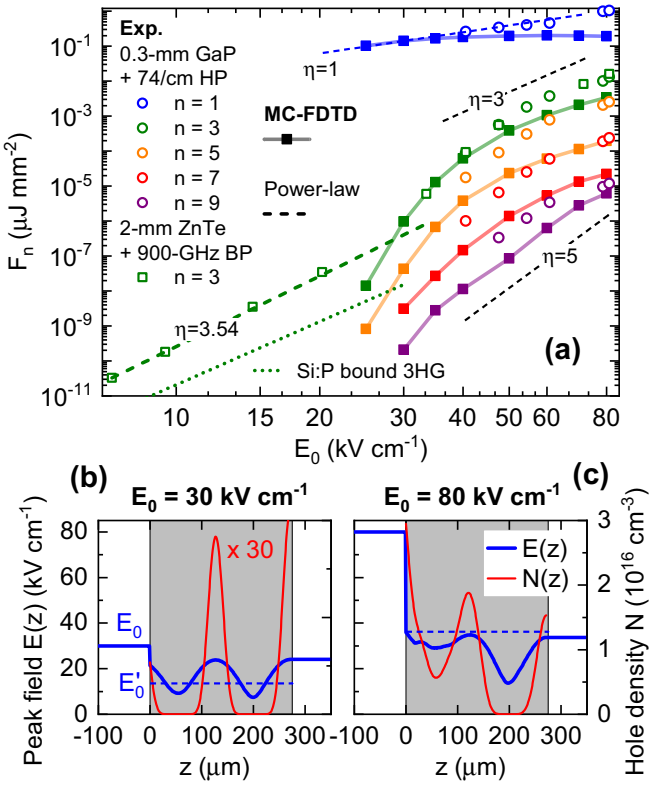

FIG. 7. (a) Pump field dependence of transmitted harmonic fluence (Sample B, $N_d = 5.0 \times 10^{16}$ cm^{-3}, $T = 4$ K, $L = 272$ μm: Experimental (open circles, with additional higher sensitivity measurements for $n = 3$ as open squares), and MC-FDTD results (filled squares, using $N_d = 5.9 \times 10^{16}$ cm^{-3}) for each odd harmonic $n = 1 - 9$. Power-law fits for $n = 1$ and $n = 3$ included as straight dashed lines (exponents η as indicated), as well as those for $\eta = 3$ and 5 as visual guides for the dependence above the photoionization threshold. See Appendix for comparison of experimental fluence results with those for $T = 300$ K [Fig. 3(a), for Sample A]. Also included is the predicted fluence for off-resonant HG from bound dopants (green dotted line, using the values for Si:P, see text). [(b),(c)] Spatial profile of peak electric field $E(t)$ and ionized hole density $N(z)$ for two values of pump field $E_0 = 30$ and 80 kV cm^{-1}, respectively. Only incident field amplitude E_0 (without reflected field) shown for $z < 0$. Also included are the nominal internal pump fields $E_0' = \hat{t}_1 E_0$ (used for the local MC simulations when specifying E_0).

(green dotted line), and is seen to be at least an order of magnitude lower than that measured experimentally.

Turning now to the higher-field range $E_0 \gtrsim 25$ kV cm^{-1}, one sees that the experimental 3HG emission grows rapidly (by more than four orders of magnitude in fluence) with a reasonably sharp onset, accompanied by the higher harmonics $n = 5, 7, 9$ almost in proportion. Indeed, the MC-FDTD simulations also show a similar pump field dependence, which is due to the onset of tunnel ionization and resultant nonlinear response of the ionized band holes, which then begins to saturate due to similar effects seen above for $T = 300$ K. Compared to the case at $T = 300$ K, here the pump field range between the ionization threshold and subsequent saturation is rather narrow, such that it is difficult to characterize power-law exponents for the higher harmonics—one sees that the growth follows approximate trends ranging between $\eta \sim 3$ to $\eta \sim 5$

in going from $n = 3$ to $n = 9$. Note that as the quasistatic tunnel ionization rate model used is expected to be only semiquantitatively correct, we omit any rescaling of the data here (as was used above in Fig. 3 where we expected near-quantitative agreement). Hence the correspondence between experiment and theory for the nonlinear harmonic fluences in Fig. 7(a) is quite striking. The importance of employing a full FDTD treatment for modeling the experimental data is demonstrated in Figs. 7(b) and 7(c), where we plot the spatial distributions of both the peak field $E(z)$ (i.e., the maximum amplitude during FDTD propagation) and photoionized hole density [after propagation, $N(z) = \Sigma_b N_b(z)$] for a value of E_0 at the onset of tunnel ionization [Fig. 7(b)] and above [Fig. 7(c)]. In Fig. 7(b), one clearly sees the standing-wave profile in $E(z)$ due to multiple reflections of the field in the sample, which manifests as three field-enhancement peaks (at each surface and in the center of the Si:B sample), which exceed the field E_0' one would have if only accounting for the Fresnel transmission coefficient $\hat{t}_1$ of the incident field E_0—this will be addressed again below in assessing the local-MC results. (Note that these effects are not significant for the $T = 300$ K case above, due to the strong, preexisting Drude absorption from the thermally ionized carriers.) This standing-wave effect also gives rise to a strong dependence of the photoionized hole profile $N(z)$, and for the case in (b) where one is still close to the initial, exponential onset of ionization, the small asymmetry in $E(z)$ manifests as a significant asymmetry in $N(z)$. For the higher-field case in Fig. 7(c), one sees that the field profile becomes more complex, affected by depletion and propagation effects, leading to a reshaping of the standing-wave pattern in $N(z)$. Moreover, the field enhancement is actually suppressed and one sees peak fields closer to the nominal value E_0'. Clearly a neglect of these effects (e.g., using a simplified, single-pass unidirectional propagation model, or a bulk layer—see below) would have a significant impact on the predicted HG emission.

One discrepancy remains. It concerns the pump-induced Drude absorption of the fundamental predicted in the MC-FDTD results [see data for $n = 1$ in Fig. 7(a)]. While the experimental transmitted fluence continues to grow linearly in the pump fluence (even showing a superlinear growth at the highest fields), for the MC-FDTD results one sees that this undergoes a significant saturation due to the Drude absorption by the ionized carriers. This manifests as a suppression of the trailing half of the pump pulse exiting the sample, as seen in the spectrogram in Fig. 6(d). We performed several test simulations to look for any possible resolution to this discrepancy: (i) reduction of the dopant density, (ii) allowing for rapid recombination of ionized holes with their parent ions (both of which would reduce the Drude absorption at ω_1); however, in all tests the agreement for the overtones was significantly degraded, with the predicted fluences F_n falling further below the experimental levels. Moreover, we tested that injection of the holes rather into the hh band does not lead to any significant changes. While the tunnel-ionization-rate model has not been tested in this regime in the literature, evidently the onset vs pump field in the simulations is close to quantitative. One possible hypothesis is that fewer holes would be generated than the employed ionization model predicts, and that there is an additional contribution to the harmonics, e.g., from recollision with their parent ions (not included in the k-space MC simulations). As presented in Sec. IV, this seems unlikely due to the strong intracycle scattering, which should strongly suppress any (coherent) recollision. An alternative explanation could be that, in the experiments, diffraction of the THz beam by the lateral variation of the photoionized hole population (and hence induced Drude response) causes off-axis components of the radiation to be imaged onto the beam axis in the EO detection crystal. As the FDTD model is based on a transverse plane-wave ansatz, this effect would not be captured in the simulations.

Proceeding on the basis that microscopic physics of the HG process are described by the MC simulations, we inspect the local response, again using MC simulations at a single z point, as summarized in Fig. 8. In Fig. 8(a), we plot the local emission intensity vs pump field for each harmonic. Also included for comparison is the scaled fluence from the MC-FDTD simulations above. One notices immediately that the threshold fields for the latter (governed in both cases by the onset of tunnel ionization) are significantly lower (by a factor $\sim$2). This is again due to the standing-wave field enhancement effect, as demonstrated by the pump field profiles shown in Figs. 7(b) and 7(c). With increasing pump fields, this field enhancement becomes increasingly suppressed, giving rise to a saturation behavior in the MC-FDTD [and, according to Fig. 7(a), also the experimental] fluence, which is not due to the inherent local response. One sees also that for the local response, the highest harmonics ($n = 7, 9$) emerge rather close to the onset of local saturation effects, which are due to similar effects for the $T = 300$ K case in Sec. III B, i.e., primarily the onset of the optical-phonon emission. However, as shown before in Fig. 7(a), the FDTD propagation effects (including phase mismatch, which becomes more severe with increasing n) result in relative harmonic yields more consistent with the experimental data.

While a comparison of the T dependence of the HG emission for the experimental results is hampered by the complex interplay of the dopant density and sample thickness, and the resultant Drude absorption and standing-wave effects for the pump field, we can make a more objective comparison here on the basis of the local MC simulations. This is shown Fig. 8(b), i.e., the data from Fig. 8(a) ($T = 4$ K) and those for $T = 300$ K [Fig. 4(a)]. As expected, while at pump fields below the photoionization threshold, the emission intensities are negligible at $T = 4$ K, for sufficiently higher pump field, the local emission *exceeds* that for $T = 300$ K. This result may at first be unexpected, given that the full population of band holes is present during the duration of the pump pulse at $T = 300$ K (see below for the time dependence of the photoionized hole populations). However, the key physical difference is that at lower T, the acoustic-phonon scattering rate is much lower [28], such that once ionized, the holes can attain higher velocities and more readily reach the threshold for optical-phonon emission, which results in a much stronger nonlinearity. Hence, while HG at $T = 300$ K is of more interest for practical applications, in principle the HG yields can be higher at $T = 4$ K for sufficiently high pump fields.

Focusing again on the results for $T = 4$ K, in Fig. 8(c) we show the relative emission intensity contribution from hh (the remaining fraction again being dominated by lh, with a

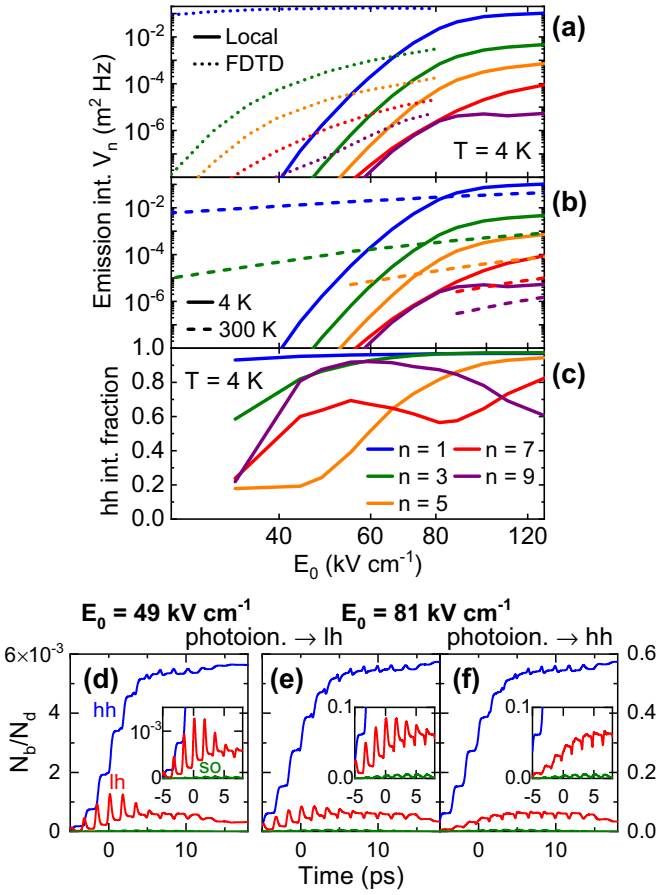

FIG. 8. Local MC results ($N_d = 5.9 \times 10^{16}$ cm^{-3}, $T = 4$ K). (a) Pump field dependence of relative emission intensities V_n for each odd harmonic $n = 1 - 9$ [solid curves, legend in (c)]. Scaled fluence from MC-FDTD [data from Fig. 7(a), here dotted curves] included for comparison. As per Fig. 4, the field values E_0 given correspond to the external incident fields [see Fig. 7(b)]. (b) Comparison of local MC results for $T = 4$ K in (a) (solid) with those for $T = 300$ K [dashed, see Fig. 4(a)], with common scale. (c) Fraction of emission intensities $r_{\mathrm{hh},n} = V_{\mathrm{hh},n}/(V_{\mathrm{hh},n} + V_{\mathrm{lh},n})$ from hh for each n vs E_0 ($r_{\mathrm{lh},n} = 1 - r_{\mathrm{hh},n}$ omitted for visual clarity). [(d),(e)] Time-dependent hole band populations (relative to N_d) for two pump fields $E_0 = 49$ kV cm^{-1} and 81 kV cm^{-1}, respectively. Initial photoionized holes are taken to enter exclusively into the lh band—see text. (f) As per (e), only using a simulation where initial photoionized holes enter exclusively into the hh band for comparison. Vertical scale for (d) at left, for (e) and (f) at right. Insets show magnified ranges.

negligible contribution from the so-band holes). Compared to the $T = 300$ K results above [Fig. 4(c), where the lh contribution was below 20% for all harmonics] here for low-pump fields, one sees that the lh contribution can actually *dominate* the HG emission for certain n, with a complex dependence on E_0, although the hh contribution becomes strongest for all n at the highest fields. To assess this intriguing result, in Figs. 8(d) and 8(e) we plot the local time-dependent hole populations $N_b(t)$ (relative to the dopant density taken as $N_d = 5.9 \times 10^{16}$ cm^{-3}), for both low and higher fields, respectively. As expected from the implementation of the photoionization model, at each intracycle peak of the pump field one sees a rapid growth in N_{lh}. Within the subsequent half-cycle, interband scattering drives the majority of the newly ionized holes into the hh band, such that during the pulse the relative densities approach those dictated by the density of states in the respective band. This intracycle interband scattering effect is specific to the case with photoionization, while the modulation of the band populations with the thermally populated bands ($T = 300$ K) is much weaker. As a control simulation, we also modified the MC treatment to rather inject all holes into the hh band, which results in the time-dependent band densities shown in Fig. 8(f). In this case, one sees that the intracycle interband scattering is weaker, and (as expected) inverted between lh and hh. Interestingly, at this high field of $E_0 = 81$ kV cm^{-1} ($E_0' = 37$ kV cm^{-1}), the predicted harmonic emission intensities are almost identical to the values for lh ionization, although the relative lh contribution decreases. Given the highly nonlinear intracycle kinetics of $N_b(t)$, in the following we inspect more closely how this might contribute to the HG emission.

One approach to analyze the relative contributions to HG emission from motion in a given band ("intraband" contribution) with that due to band-population changes ("interband" contribution), is to calculate the (occupation-weighted) acceleration components, i.e., with $v(t) = \Sigma_b n_b(t) v_b(t)$ (where $n_b = N_b/N_d$ is the density of ionized holes in band b relative to the dopant density) one obtains $\dot{v} = \partial_t v = \Sigma_b(\dot{v}_b^{(\mathrm{B})} + \dot{v}_b^{(\mathrm{IB})})$, where $\dot{v}_b^{(\mathrm{B})} = n_b \dot{v}_b$ and $\dot{v}_b^{(\mathrm{IB})} = \dot{n}_b v_b$. In this case, $\dot{v}_b^{(\mathrm{IB})}$ comprises both the contributions from photoionization ("generational nonlinearity") and from hh ↔ lh scattering. Although our physical situation differs from the well-studied HG process from dissociated e-h pairs [29–31], this is reasonably consistent with the terminology introduced there. While this definition tacitly assumes that carriers entering a band adopt the ensemble average velocity in that band $v_b(t)$, in the absence of a more rigorous treatment one at least observes that $\dot{v}_b^{(\mathrm{IB})}$ vanishes for $\dot{N}_b(t) = 0$, while the occupation weighting provides a direct measure of the relative contribution from each band. By applying a band-pass filter about each harmonic frequency ω_n, we can inspect their respective contributions to each harmonic. This is presented in Fig. 9 for both a low (onset of photoionization) and high (saturation regime) pump fields for both hh and lh bands. Beginning with the low-field case [Fig. 9(a), $E_0 = 49$ kV cm^{-1}], several features can be observed in the results. Firstly, one sees that the lh contribution is significant, and even dominates the HG emission for $n = 5$ {as seen in Fig. 8(c) for this field value, noting that the emission intensity scales with $[v(t)]^2$}. Moreover, for the lh band, $\dot{v}^{(\mathrm{IB})}$ is comparable or even somewhat larger than $\dot{v}^{(\mathrm{B})}$, depending on n. Hence the interband contribution at low-pump fields plays in important role in the HG emission, especially around the temporal peak ($t = 0$ ps) of the pump pulse. In contrast, for the higher-field case [Fig. 9(b), $E_0 = 81$ kV cm^{-1}], the hh contribution is significantly larger for all harmonics, as is the contribution from $\dot{v}^{(\mathrm{B})}$, i.e., the HG emission is dominated by the EDS of the hh after they have entered the band, similar to the $T = 300$ K case (although the lower temperature here also affects the acoustic-phonon scattering rates and equilibrium Fermi-Dirac distribution).

Finally, we address the evolution of the carrier distribution (both along k_x parallel to the pump field, and transversely

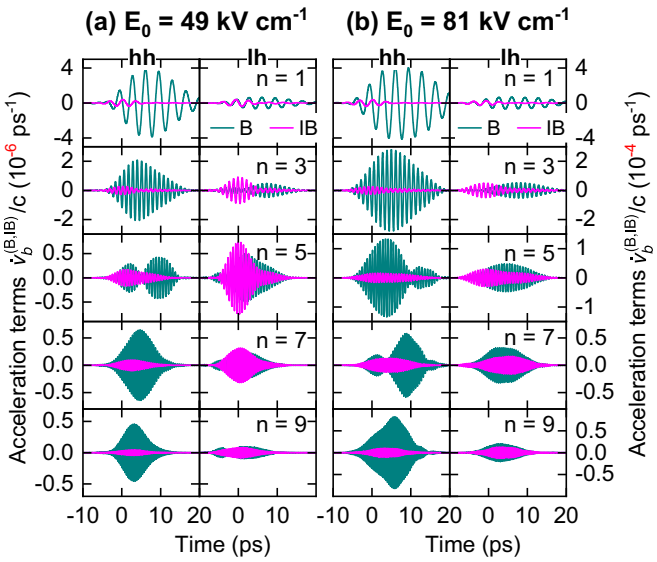

FIG. 9. Local MC results ($N_d = 5.9 \times 10^{16}$ cm^{-3}, $T = 4$ K). Decomposition of (occupation-weighted) hole acceleration into "intraband" ($\dot{v}_b^{(B)}$) and "interband" ($\dot{v}_b^{(IB)}$) contributions (see text for definitions) for (a) $E_0 = 49$ kV cm^{-1} and (b) $E_0 = 81$ kV cm^{-1}, for each band ($b =$ hh, lh), filtered for each harmonic n. Note different vertical scaling in (a) and (b).

along $k_{y,z}$) and the real-space trajectories of photoionized holes, as predicted by the local-MC simulations. We consider only the high-field case. In Figs. 10(a) and 10(b), we plot the time evolution of the ensemble-averaged wavevector $k_x(t)$ (separately for hh and lh), along with the rms spreads $\sigma_x(t)$ (along k_x) and $\sigma_{y,z}(t)$ (along $k_{y,z}$), for both the (a) room-temperature ($T = 300$ K, Sec. III B) and (b) low-temperature ($T = 4$ K) situations. For $T = 300$ K, one sees again the relatively broad distribution before the pump pulse, due to the thermal Fermi-Dirac distribution, as discussed above in connection with Figs. 4(e) and 4(f), whose displacement/spread is only moderately perturbed during the pump excitation. This is in contrast to the case we simulated in Ref. [1] for $T = 10$ K (assuming a small density of thermally ionized carriers) where $\sigma_j < 0.01(2\pi/a)$ (for all $j = x, y, z$) before the pulse, and grew significantly during the pulse (although remaining somewhat smaller than the amplitude of k_x), as here the relative heating of the hole ensemble is small compared to $k_B T$. For the case of $T = 4$ K in Fig. 10(b), with holes generated by photoionization, one sees that the spread σ_j rapidly acquires a comparable magnitude as for $T = 300$ K, which is caused by rapid scattering processes even during the first half-cycle of the pump wave following respective ionization of each hole, with the spread $\sigma_{y,z}(t)$ pursuing $\sigma_x(t)$ closely due to transverse scattering events. Although we defer the discussion of subsequent recollision of ionized holes with their parent ions to the next section (see Sec. IV B), we show here in Fig. 10(c) results for the distance $r = |\vec{r}_h - \vec{r}_{B^-}|$ between holes and their parent ions following ionization (608 holes tracked in total). One can see clearly the coherent bursts of new holes about the field peak of each pump half-cycle, and the ballistic initial acceleration to distances $r \sim 50$ nm, which then becomes diffuse due to momentum scattering, although one can still perceive a

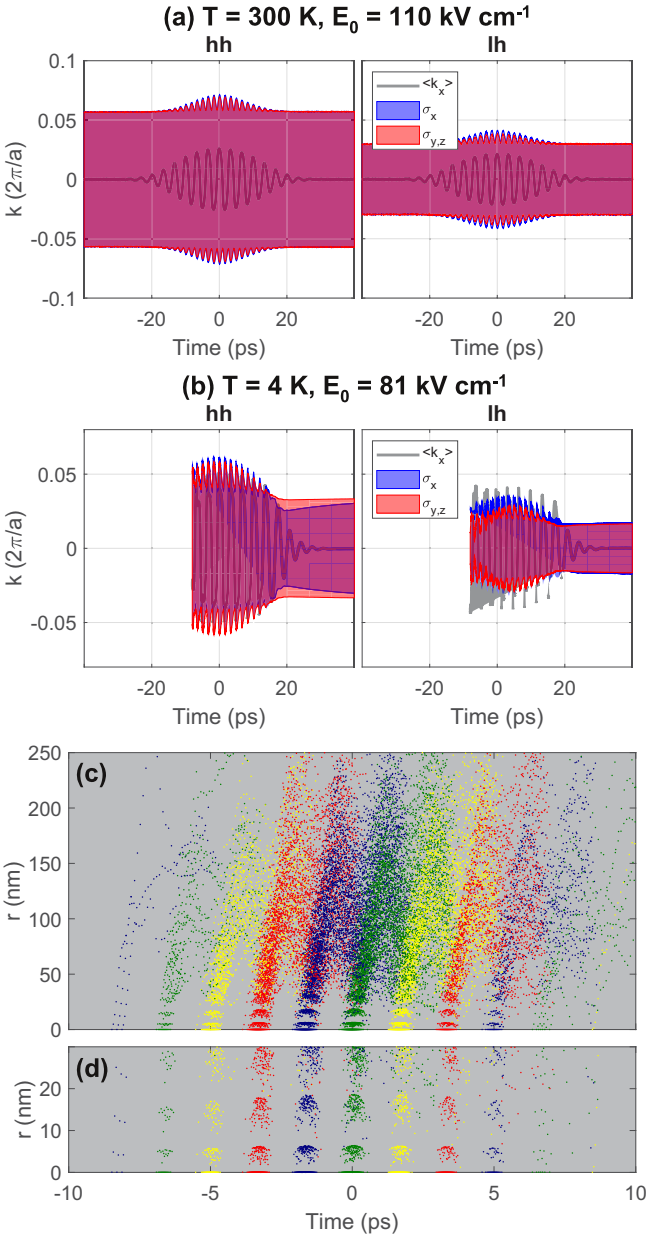

FIG. 10. Time-dependence of k-space distributions from local-MC simulations for (a) $T = 300$ K and (b) $T = 4$ K, for both hh (left panels) and lh (right panels), including ensemble average $k_x(t)$ (parallel to pump field), and rms spreads $\sigma_x(t)$ (along k_x) and $\sigma_y(t) = \sigma_z(t)$ (along $k_{y,z}$). In (b), data truncated at early times before sufficient photoionized holes exist to perform statistics. (c) Time-dependent distance of hole from parent ion for the case in (b) (hh and lh combined), obtained by integrating $v_g(t)$ for each particle (608 holes in total, data only for the first 3 ps after respective ionization of each hole, downsampled to a time step of 50 fs for the first 500 fs, and 100 fs thereafter). Color coding for each burst of photoionized holes during each pump half-cycle. (d) Vertical zoom of (c) to allow inspection of small number of holes returning to parent ion during subsequent half-cycles.

wave-like trend in each half-cycle as the holes accelerate back in the direction of their parent ions. To inspect for possible recollision, in Fig. 10(d) we plot a vertical zoom of the data in (c). A close inspection (in particular for the half-cycles

in the range of a few ps about $t = 0$ where one has ∼100 ionized holes/burst) shows that a small fraction do return to distances $r < 30$ nm, although very few $r < 10$ nm, as the transverse momentum acquired from scattering causes them to pass $x = 0$ displaced from $y = z = 0$ (the same applies for holes returning after two half-cycles from the opposite x direction). Hence scattering is seen to seriously degrade the probability of a close recollision for the ionized holes. The fact that the first near-recollisions occur close to a *half*-cycle after ionization might at first seem unexpected, as it is well known from the semiclassical treatment of gas-phase recollision [20] that ionized charges created close to the field peaks, following the ballistic equation $\partial_t v = qE(t)/m$, return after a *full* cycle. However, one can show for the case with scattering, e.g., taking a simple constant damping rate Γ [$\partial_t v = qE(t)/m - \Gamma v$], that the holes indeed reapproach their parent ions after a half-cycle for $\Gamma \ll \omega_1$ (see Appendix).

In this section, we could account for the HG emission from band holes, following photoionization of bound dopants and the subsequent band-carrier dynamics. The standing wave effects for the pump pulse lead to a lower pump field threshold than expected (due to field enhancement peaks within the sample). Local MC results indicate that the HG emission yields at $T = 4$ K can indeed exceed those at $T = 300$ K, due to the suppression of acoustic-phonon scattering, allowing the photoionized band carriers to more readily reach the threshold energy for optical-phonon emission. A theoretical analysis of the HG emission due to nonlinear motion in the band compared to the currents associated with initial photoionization into the bands and interband scattering showed that the latter are also significant close to the ionization threshold. However, intracycle scattering should strongly suppress any emission due to recollision of ionized holes with their parent ions.

IV. DISCUSSION

A. Comparison with harmonic generation in graphene

We first address the magnitude of the band nonlinearities determined for the experiments at $T = 300$ K [Sec. III B, Fig. 3(c)]. Here we compare these values of $\chi^{(n)}$ with those determined recently for graphene [2,32], where the HG mechanism was attributed to an intracycle instability in the Drude heating/absorption of the carrier distribution. Taking the effective thickness of the monolayer as $L_g = 0.3$ nm, the authors deduced values $\chi^{(n)}$ (in respective SI units, $\mathrm{m}^{(n-1)}\,\mathrm{V}^{-(n-1)}$) of 1.7×10^{-9} ($n = 3$), 1.2×10^{-22} ($n = 5$), and 1.7×10^{-38} ($n = 7$). While the value of $\chi^{(3)}$ is four orders of magnitude higher than our present case, this is essentially due to the fact that graphene is an extremely potent electronic system, where the 2D carrier density in [2] (due to substrate-induced electrostatic p-doping) of $N_{2D} = 2.1 \times 10^{12}$ cm^{-2} is concentrated in a single monolayer. If we normalize the nonlinear coefficients to the 3D carrier densities N_d (Si:B) and $N_g = N_{2D}/L_g$ (graphene), one arrives at $\chi^{(3)}/N_d = 1.7 \times 10^{-35}$ m^5 V^{-2} and $\chi^{(3)}/N_g = 2.4 \times 10^{-35}$ m^5 V^{-2}, i.e., the nonlinear response per carrier is almost equal. One also notes that the ratios between successive $\chi^{(n)}$ values ($n = 3 : 5 : 7$) are also loosely correlated, in SI units $\sim 1 : 10^{-14} : 5 \times 10^{-14}$ for Si:B, and $\sim 1 : 7 \times 10^{-14} : 10^{-16}$ for graphene. It is hence not correct to conclude that the unique band structure of graphene would lead directly or indirectly to a stronger nonlinear response per charge carrier as compared to conventional semiconductors. While beyond the scope of the current paper, this comparison raises the interesting question whether a more universal sum-rule [33,34] may apply for the (odd-order) THz nonlinear susceptibilities of charges in solid-state bands.

B. Contribution of recollisions to the nonlinear response?

We turn now to the low-temperature HG process with photoionization. As mentioned in Sec. III C, one can compare our scenario with that of the more well-established HG process observed for electron-hole pairs in solids with an energy bandgap, following interband excitation via either tunnel ionization [29,30,35,36] or optical preexcitation [31,37]. These studies provide strong support for recollision as a dominant mechanism for HG emission (in that context referred to as "interband" generation), despite the presence of scattering processes, although the role of the subsequent anharmonic "intraband" currents are also proposed to dominate, at least in certain regimes [38].

In the case with pump fields at mid-infrared or higher frequencies (and hence carrier periods <50 fs), it seems reasonable that such a coherent recollision can occur for a significant fraction of the e-h pairs. Nevertheless, even for recollision of e-h pairs (arising from tunnel ionization of optically excited excitons) in GaAs/AlGaAs quantum wells [31] with a 570-GHz driving field, the authors deduce that LO phonon emission there does not destroy the recollision process as the required kinetic energy ($\mathcal{E}_{op} = 36$ meV) is only acquired during a short time directly before recollision. Note that this is based on the assumption that the dominant trajectory for a given emitted photon energy $h\nu_{em}$ corresponds to *complete* e-h recombination, i.e., $h\nu_{em} = I_p + \mathcal{E}_r$, where the kinetic energy upon recollision $\mathcal{E}_r$ is governed by their birth time in the driving field. This assumption is deduced from the condition for coherent emission in the purely ballistic case, as in dilute gases [20], and may well need revision when stochastic scattering processes occur such that the trajectories are no longer deterministic.

Our photoionization+MC results [Sec. III C, Fig. 10(c)] suggest that the scattering processes occurring during the hole trajectories severely disrupt the return paths to their parent ions (both in terms of proximity and coherence). A simple treatment of the scattering (see Appendix) also indicates its decisive role, as it results in a kinetic energy $\mathcal{E}_r$ during any residual recollision events lower than $0.1 \cdot U_p$, compared to $3.17 \cdot U_p$ for the ballistic case (U_p being again the ponderomotive energy, see second paragraph of Sec. III C). We note in passing, that this should not result in a high-frequency cut-off of HG in the frequency range covered in this study (4 THz), as that cut-off in the emission photon energy is given by $I_p + \mathcal{E}_r$, where the ionization energy $I_p = 45$ meV$\hat{=}$ 10.9 THz is already above the covered photon energy range.

Nevertheless, given that the MC simulations here underestimate the HG emission strength [Fig. 7(a)], further theoretical studies should aim at quantifying any residual HG from recollision. More generally, the results here strongly motivate future efforts to refine the description of the photoionization

and any interactions with the parent ions. While we have employed the literature static-field ionization rate and initially populated only the lh band [21,22], this approach should be compared to time-dependent quantum-mechanical treatments, e.g., propagating the time-dependent density-matrix (or semiconductor-Bloch) equations [37,39–41]. Such simulations may require a detailed treatment of both (i) the excited bound acceptor states [42] if these are involved as intermediate states during ionization [39,43], and (ii) the subsequent scattering processes occurring in the bands (where our MC treatment here does include explicitly effects such as the angular dependence and Pauli blocking).

V. CONCLUSIONS

In conclusion, we have presented a combined experimental and theoretical study of harmonic generation in Si:B with multicycle high-field THz pump pulses, for both temperature regimes where the band holes are either initially thermally ionized ($T = 300$ K), or photoionized during the pulse ($T = 4$ K). Pumping at 300 GHz, we observed up to the ninth harmonic order at room temperature and up to at least the 11th order at cryogenic temperature. Near quantitative agreement with experiment was achieved with Monte Carlo simulations, but only when one includes both lh and hh bands and treats the propagation effects rigorously. This agreement allowed us elucidate the microscopic harmonic generation processes on the basis of simulations of the local dynamics, which showed that the nonlinear response of preexisting holes are dominated by energy-dependent scattering (and not band nonparabolicity) in this excitation regime, whereas for photoionized holes, the initial interband scattering processes also play an important role, especially close to the ionization threshold. We find that scattering during the first subcycle should strongly influence the trajectories of photoionized holes (and any coherent recollision with their parent ions), which strongly motivates further studies of the photoionization process and subsequent interactions with the parent ions for the case of harmonic generation in solids. Here, THz pump THz-probe (and/or photocurrent-probe) experiments would also be invaluable.

The nonlinear susceptibility per charge carrier was shown to be comparable to that for harmonic generation in graphene. While the nonlinear response in graphene is indeed attributed to a different physical mechanism (intracycle carrier temperature modulation), this shows that the Dirac-type band structure apparently does not lead to an inherently higher per-carrier nonlinear response than that found for band carriers in Si.

To increase the harmonic yields for practical applications at room temperature, one needs to consider how to circumvent the Drude absorption/reflection, which would result from higher dopant densities or longer propagation distances. Here one could consider the use of waveguides with a thin, doped top layer, and/or combine this with resonator schemes, with the ultimate aim to realize a new platform for Si-based free-space/on-chip frequency multipliers or frequency-comb generators for pump electric fields even lower than 10 kV cm^{-1}.

We finally note that this paper serves to validate the application of MC simulations at this level of description for even higher frequencies and field strengths than it was previously employed, which will become increasingly relevant for the description of future (opto-)electronic devices.

ACKNOWLEDGMENTS

We acknowledge funding by the German Research Foundation (DFG) under the contract RO 770/41 and via the Collaborative Research Center TRR 288 (422213477, Project No. B08). Parts of this research were carried out at the ELBE Center for High-Power Radiation Sources at the Helmholtz-Zentrum Dresden - Rossendorf e. V., a member of the Helmholtz Association; for more information about the facility, see Ref. [44]. The authors thank Alexej Pashkin for his help with experiments, and the ELBE team for the operation of the TELBE facility.

APPENDIX

1. Experimental setup

The detailed experimental setup can be found in Fig. 11.

2. Pump- and EO-detected-field calibration

The pump fields E_0 were calibrated by first measuring the average power $\bar{P}$ (with a commercial, calibrated THz power-meter, Ophir 3A-P-THz) and beam intensity profile in free-space at the sample position $\bar{I}(x, y)$ (using a commercial pyroelectric camera, Ophir Pyrocam III), the latter yielding beam FWHM of $w_{1/2} = 560$ μm (for the experiments at $T = 300$ K including the additional teflon lens) and $w_{1/2} = 850$ μm (for the experiments at $T = 4$ K with the sample mounted in the cryostat). The pump pulse fluence is then given by $F_0 = \frac{J_0}{\pi w^2/2}$ where $J_0 = \bar{P}/\nu_p$ (repetition rate $\nu_p = 50$ kHz) and $w = w_{1/2}/\sqrt{2\log 2}$, which combined with

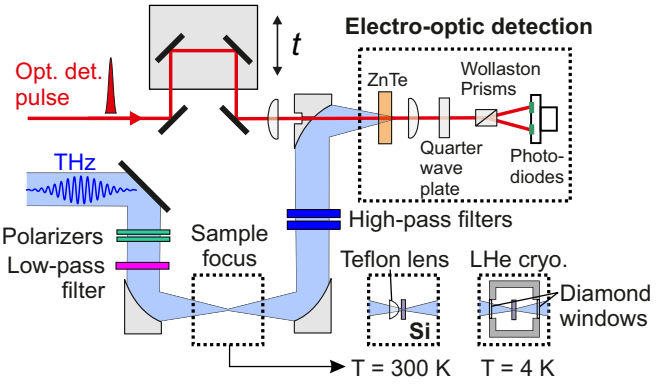

FIG. 11. Schematic of experimental setup with time-domain electro-optic detection of TELBE THz pulses after transmission through Si:B sample, either at $T = 300$ K (with an additional teflon lens for tighter focusing and incident fields exceeding 100 kV cm^{-1}) or $T = 4$ K (sample in cryostat). Before sample: Pump field controlled by relative rotation of polarizer-pair; TELBE source-harmonics suppressed by low-pass filter. Following sample: High-pass filter (HPF) used to balance relative intensity of fundamental and harmonics—see Sec. VI B below for details on correction for HPF transmission, and EO response function for the two crystals used.

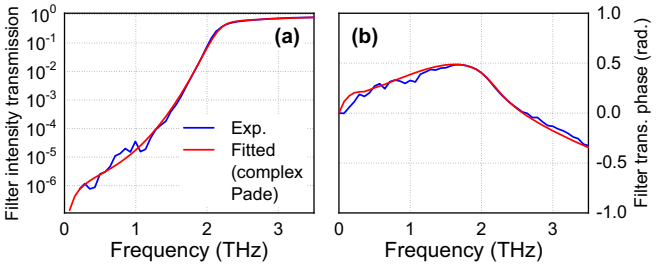

FIG. 12. Measured characteristics of high-pass filter following Si:B sample to avoid saturation of EO signals by fundamental. Transmission (a) intensity and (b) phase, as determined by a combination of THz-TDS and FTIR measurements, including a model fitted curve used for the numerical correction of spectra (based on a complex Pade rational fit).

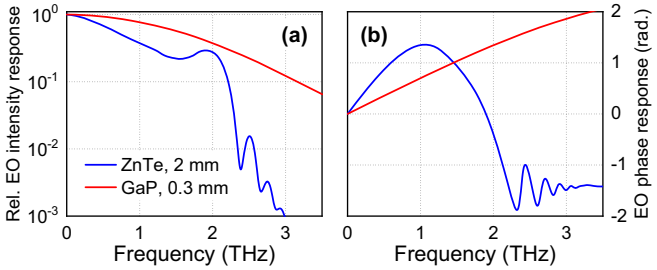

FIG. 13. Calculated relative EO (a) intensity and (b) phase response for the two crystals (see legend) used in the experiments, and used to numerically correct the emission spectra.

the EO temporal field profile allows one to calculated the peak pump fields. The reduced pump field as the crossed polarizers are rotated (relative angle θ) was then calculated via $E_0 \rightarrow E_0 \cos^2\theta$—this being cross checked by comparing the EO signals in the linear transmission regime of the Si:B samples.

The calibration of the detected EO fields required firstly correction of the spectral intensity/phase for (i) the high-pass filter transmission/phase after the samples, and (ii) the relative EO response of the detection crystals used. Thereafter, the absolute field could be calibrated by scaling the fundamental EO signal (measured in the linear transmission regime, for $T = 300\,\mathrm{K}$ with an undoped sample) to the known pump values E_0 and accounting for the Fresnel transmission coefficients at the sample interfaces and etalon interference (cross checked with linear FDTD simulations).

High-pass filter transmission (QMC Instruments Ltd, HP74 cm^{-1}): Here we combined both THz-TDS and far-infrared Fourier spectrometry measurements to determine the transmission intensity and phase of the filter used, as shown in Fig. 12.

Electro-optic response: As the absolute field strengths were calibrated using the known pump field E_0 (see above), one must only correct the spectra for the relative intensity/phase of the two EO sensors used. The EO response function $R(\Omega)$ between measured signal $S(\Omega) = \mathcal{F}\{S(t)\} = R(\Omega) \cdot E(\Omega)$ and incident on-axis THz field $E(\Omega)$ can be derived as [45,46]

$$R(\Omega) \propto \chi^{(2)}(\omega_0, \Omega) \int_{-\infty}^{\infty} P(\Omega, \Omega') E_0(\Omega') E_0^*(\Omega + \Omega') \quad \text{(A1)}$$

where $P = (e^{i\Delta k L} - 1)/i\Delta k$, $\Delta k(\Omega, \Omega') = k^*(\omega_0 + \Omega + \Omega') - k(\omega_0 + \Omega') - k(\Omega)$, in terms of the complex wavenumbers of the THz and optical (E_0) fields, crystal length L. Here we take $\chi^{(2)}$ as approximately constant (as it only varies significantly approaching close to the respective phonon frequencies, sufficiently above our range for the HG emission). While a common simplification is to evaluate the integral in Eq. (A1) at the optical center frequency, this results in sharp artifacts in $R(\Omega)$, which are indeed smoothed out when calculating the correct convolution over the optical spectrum. One can evaluate the integral over P (assuming a Gaussian optical pulse $E_0 = E_{00} e^{-t^2/T_0^2}$, where here $T_{1/2} = \sqrt{2\log 2} \cdot T_0 = 100$ fs). The resulting relative intensity $|R|^2$ and phase $\arg R$ response are shown in Figs. 13(a) and 13(b), respectively, for the two EO crystals used (see legend), using literature data [47,48] for the THz/optical refractive indices and absorption coefficients to calculate k. For the case of the 300-μm-thick GaP crystal, the response roll-off in this range is dictated mostly from the finite optical pulse duration.

3. Si:B samples: Selection and doping determination

For the room-temperature experiments, we employed a Si:B sample grown in the [001] direction by the float-zone method with doping by boron from the melt. As a compromise between free-carrier absorption (and dopant interactions) vs achieving a sufficiently strong HG emission, we chose a moderately low doping density 5.75×10^{15} cm^{-3} (as determined by four-point DC resistivity measurements) and rather large thickness ($L = 900$ μm), The samples were cut to parallelepipeds with lateral dimensions $7.1 \times 7.1\,\mathrm{mm}^2$, followed by optical polishing of the entry/exit facets.

Since the HG emission was weaker at low temperature (i.e., for pump fields at/below the onset of photoionization), in order to increase the signal levels, we employed a commercially obtained sample (from MTI Corp.) with ~10 times higher doping density (and thickness $L = 272$ μm, determined from spectral interference fringes). Here, we calibrated the dopant density using a THz-TDS measurement at $T = 200\,\mathrm{K}$ (sufficiently high that all dopants are thermally ionized). We then fit the transmission spectrum over the range 2–7 THz using a

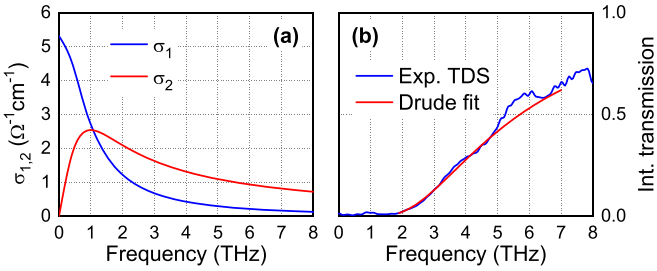

FIG. 14. (a) Generalized Drude conductivity spectrum for Si:B Sample B used for experiments at $T = 4\,\mathrm{K}$, from MC simulations [at $T = 200\,\mathrm{K}$ using the fitted value of $N_d = 5.0 \times 10^{16}$ cm^{-3} in (b)]. (b) Experimental intensity transmission spectrum of sample, and fitted spectrum using the conductivity model in (a).

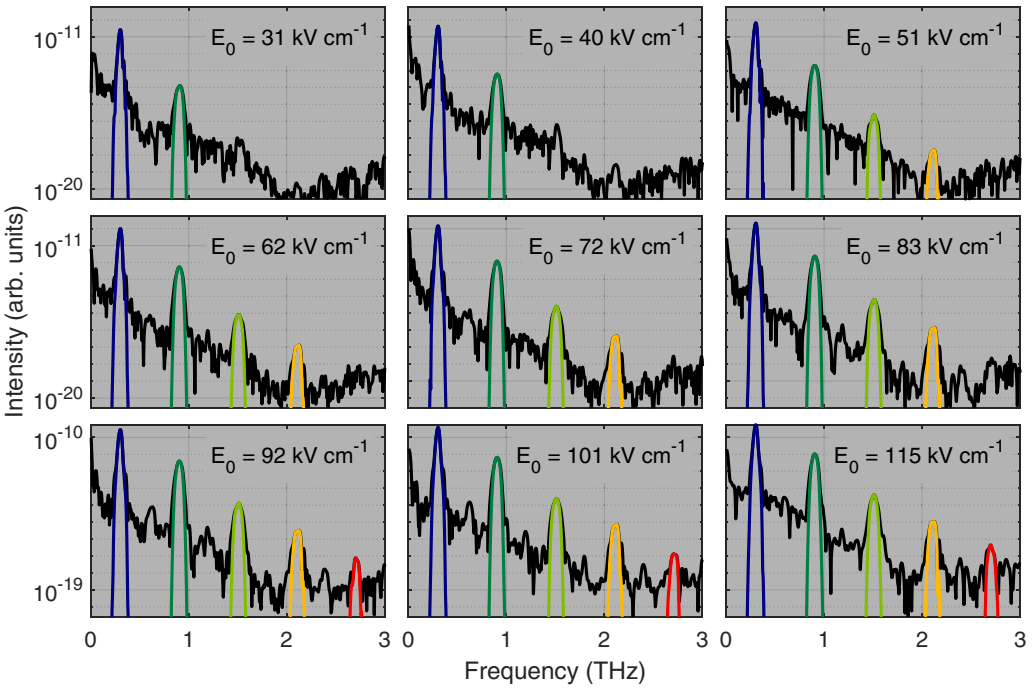

FIG. 15. Experimental intensity spectra and filtered odd harmonics ($n = 1 - 9$) for each pump field E_0 ($T = 300$ K, Sample A, $N_d = 5.75 \times 10^{15}$ cm^{-3}, $L = 900$ μm).

generalized Drude model, using the predicted Drude response from MC simulations [15,16], which yielded a best estimate of $N_d = 5.0 \times 10^{16}$ cm^{-3}. These results are summarized in Fig. 14.

4. Room-temperature HG: Time-domain fields and spectra

In Fig. 15 we plot the intensity spectra and filtered harmonics for the experiments at $T = 300$ K, obtained by applying a super-Gaussian filter $F_n(\nu) = \exp(-[(\nu - \nu_n)/\delta\nu]^\eta)$ with $\eta = 4$ and $\delta\nu = 50$ GHz. The corresponding filtered time-domain fields are shown in Fig. 16.

5. Room-temperature HG: Pump field dependence

In Fig. 2 of the main paper, we plot a comparison of the experimental and MC-FDTD peak fields vs pump field E_0 after applying rescaling to the experimental data, i.e., $E_0 \rightarrow$

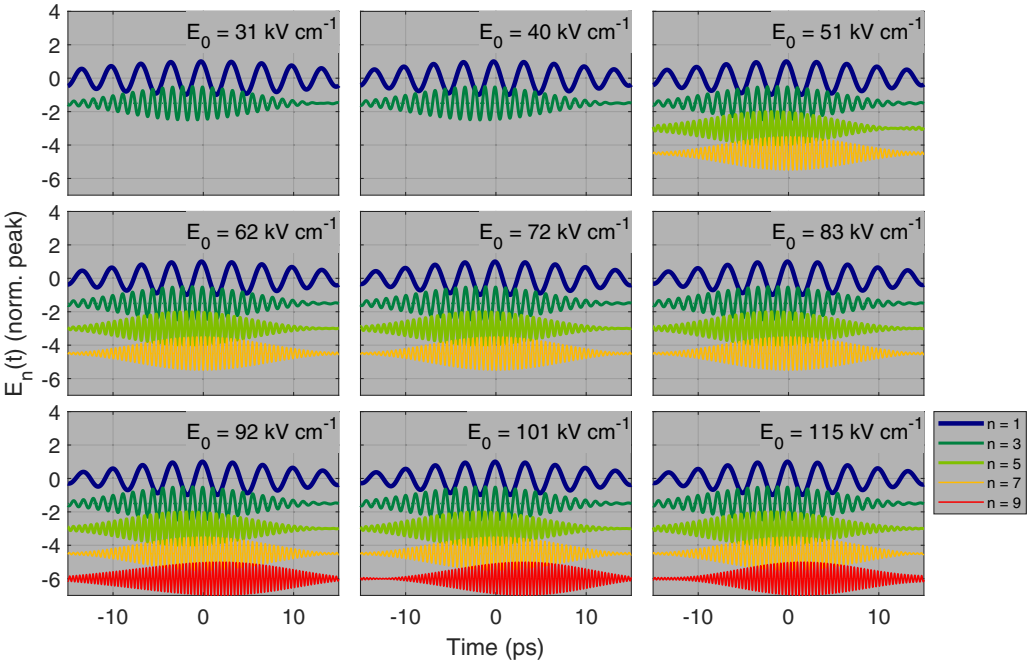

FIG. 16. Normalized experimental time-domain fields for each filtered harmonic in Fig. 15 ($T = 300$ K, Sample A, $N_d = 5.75 \times 10^{15}$ cm^{-3}, $L = 900$ μm).

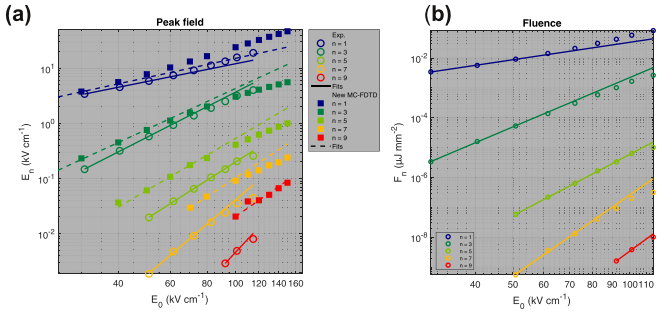

FIG. 17. (a) Pump field dependence of transmitted harmonic peak fields (Sample A, $N_d = 5.75 \times 10^{15}$ cm^{-3}, $T = 300$ K, $L = 900$ μm): Experimental results (open circles), and MC-FDTD results (crosses) for each odd harmonic $n = 1 - 9$. Respective power-law fits included as straight lines. (b) Corresponding experimental harmonic fluence F_n.

$0.9 \cdot E_0$ for the pump field as well as moderate scale factors for the emitted 5HG, 7HG and, 9HG fields E_n. This was done to aid visual comparison, and may point either to some issues with the experimental field calibration (despite the efforts made in Sec. VI B above, or a small systematic discrepancy in the MC-FDTD description). For completeness, we plot in Fig. 17(a) a comparison of the data without the rescaling. In Fig. 17(b), we also show the raw experimental fluence values [$F_n = \epsilon_0 c \int dt E_n^2(t)$], which reflect the same behavior as the peak field data E_n, i.e., pulse-shape effects do not play an important role for quantifying the dependence on pump field.

6. Room-temperature HG: Relative phases of harmonics vs pump field

Besides an analysis of the harmonic peak fields (or emission fluence), another probe of the HG process that can be extracted from the experimental/simulated emitted fields is their phases φ_m relative to the fundamental wave. Note that care should be taken in defining/interpreting such phases, as for waves of different frequency, this is not objectively defined [e.g., extracting the spectral phase $\varphi_n = \varphi(\omega_n)$ from Fourier spectra will depend on the choice of time origin]. One can inspect the temporal shift between a intracycle field peak position t_1 of the fundamental wave and the nearest peak t_n for the waves with $n > 1$. Hence $\Delta t_n = t_n - t_1$ would be constant if the harmonics all followed an ideal, instantaneous, local, nonlinear response. However, propagation effects (Drude dispersion and the resultant phase-mismatch) will again distort these phase relationships, as we confirmed with a series of FDTD simulations vs sample thickness L, using a simplified, instantaneous Caughey-Thomas response [49] with $\mu_0 = 484$ cm^{-2} V^{-1} s^{-1}, $v_{sat} = 10^7$ cms^{-1}, and $\beta = 2$, instead of MC dynamics. Hence even the values Δt_n do not deliver an objective measure for the phase of the *local* nonlinear response. Nevertheless, one can compare the pump field dependence between experimental and MC-FDTD simulation results to further inspect how quantitative the MC-FDTD description is.

A comparison of the experimental and MC-FDTD phases is shown in Figs. 18(a) and 18(b). As can be seen in (a), there is a well-defined pump field dependence for each harmonic,

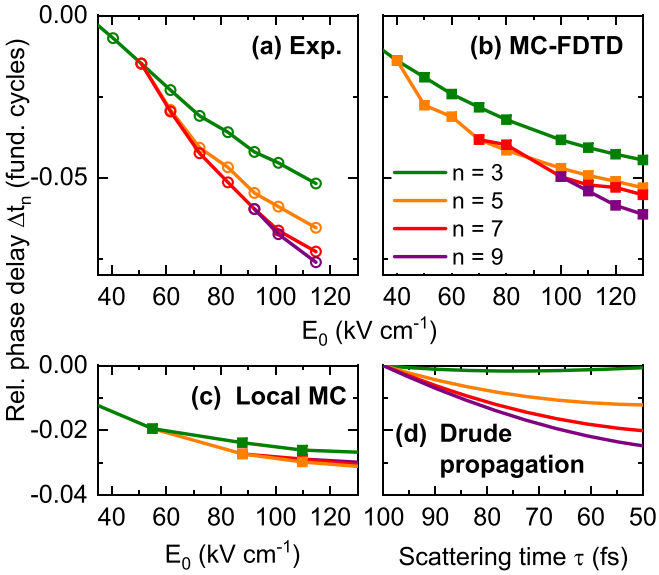

FIG. 18. Pump dependence of the relative phases of emitted harmonics, expressed as the temporal shift between intracycle field peaks $\Delta t_n = t_n - t_1$ of each harmonic relative to the fundamental, about the peak of the fundamental envelope. To aid comparison, we also set $\Delta_n(E_0) \to \Delta_{n-2}(E_0)$ at each field E_0 where successive harmonics n have sufficient signal-to-noise to begin extracting the phase. (a) Experimental, (b) MC-FDTD, and (c) local-MC simulation results. (d) Relative phase delay due to linear propagation ($L = 900$ μm) assuming a Drude model with constant effective mass vs scattering time τ.

with a negative relative phase delay with increasing E_0, the magnitude of the slope growing with n. The MC-FDTD results in (b) are seen to be qualitatively in agreement, with a somewhat reduced range for the variation. In order to assess the cause for this trend, in Fig. 18(c) we plot the corresponding local MC results. These show the same sign for the field dependence, but with a significantly smaller magnitude, which is only weakly dependent on n. To assess possible propagation effects, in Fig. 18(d) we plot the phase delay expected for linear propagation with a Drude model for the holes, as a function of the Drude scattering time τ (with a constant effective mass corresponding to $\sigma_0 = 0.4\ \Omega^{-1}$cm^{-1} for $\tau = 100$ s^{-1}).

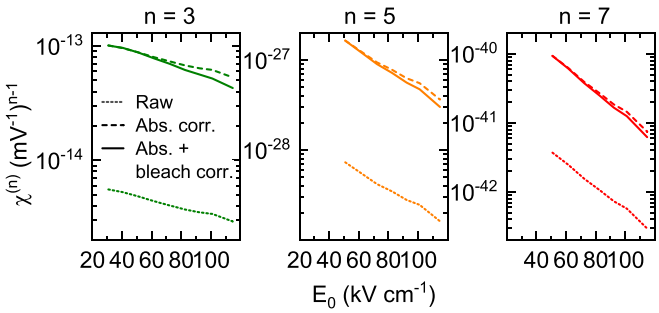

FIG. 19. Estimated nonlinear susceptibilities vs pump field E_0 for $n = 3, 5, 7$, based on the raw data (dotted lines), correction for Drude absorption (dashed), and fine correction for absorption bleach of the pump at high fields (Sample A, $N_d = 5.75 \times 10^{15}$ cm^{-3}, $T = 300$ K, $L = 900$ μm).

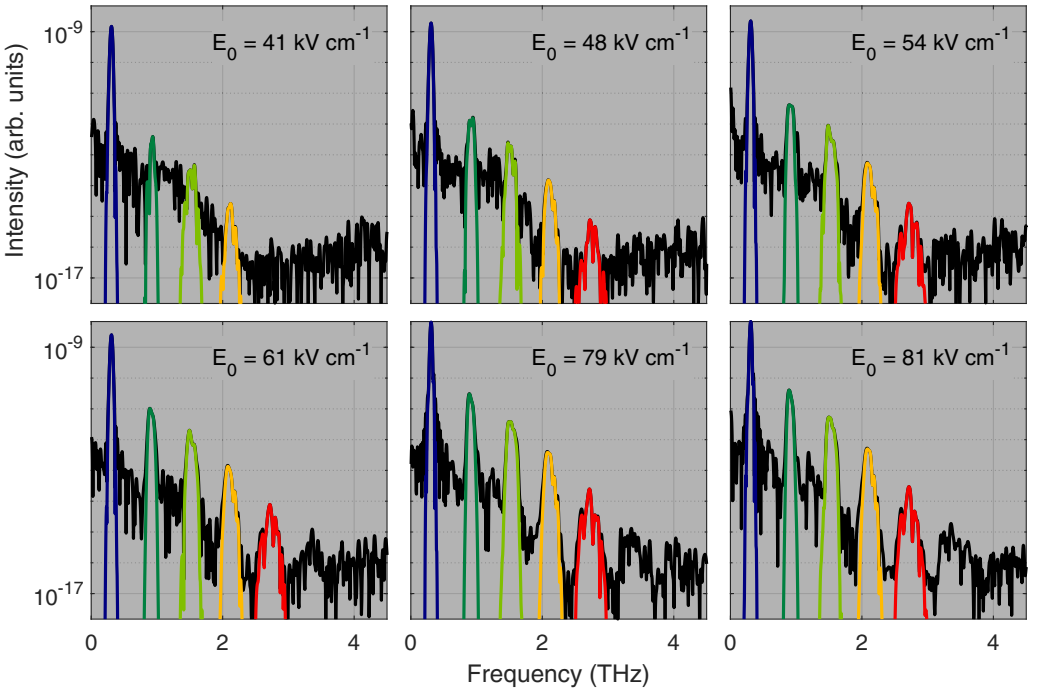

FIG. 20. Experimental intensity spectra and filtered odd harmonics ($n = 1 - 9$) for each pump field E_0 ($T = 4$ K, Sample B, $N_d = 5.0 \times 10^{16}$ cm^{-3}, $L = 272$ μm).

This should reflect qualitatively the effect of increasing scattering rate vs E_0 seen in the MC simulations (see main text). Here one sees a similar qualitative trend, only with a stronger dependence on n. One can trace this back to the change in the Drude conductivity spectrum, and hence refractive index, with decreasing τ: this leads to a decrease of $\sigma(\omega)$ at low frequencies, which reduces the negative dispersion and causes the phase velocity to decrease. Hence the phase advance of the harmonics seen in Fig. 18(d) is primarily due to the retardance of the fundamental wave. The combined effects of the phase shift in the local-MC phase shifts (which result from the nontrivial carrier dynamics) and such a propagation effect result in the stronger total phase shift variation seen in Fig. 18(b).

7. Room-temperature HG: Correction of $\chi^{(n)}$ estimation for Drude absorption

As described in the main text, for the estimate of the nonlinear susceptibilities $\chi^{(n)}$, one must correct for the Drude absorption α_n of the pump and harmonics (see main paper for the correction terms). As there is a small bleach of the Drude

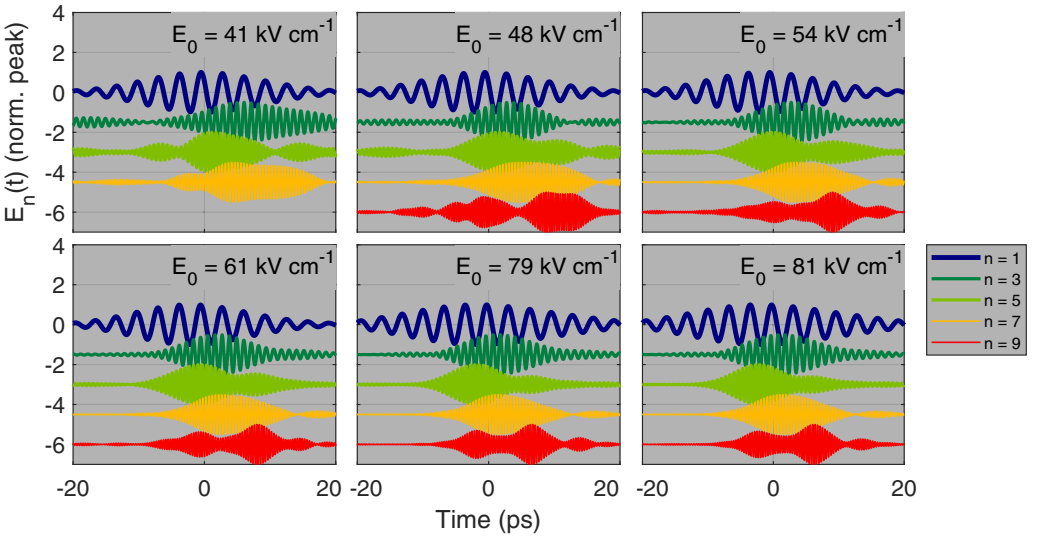

FIG. 21. Normalized experimental time-domain fields for each filtered harmonic in Fig. 20 ($T = 4$ K, Sample B, $N_d = 5.0 \times 10^{16}$ cm^{-3}, $L = 272$ μm).

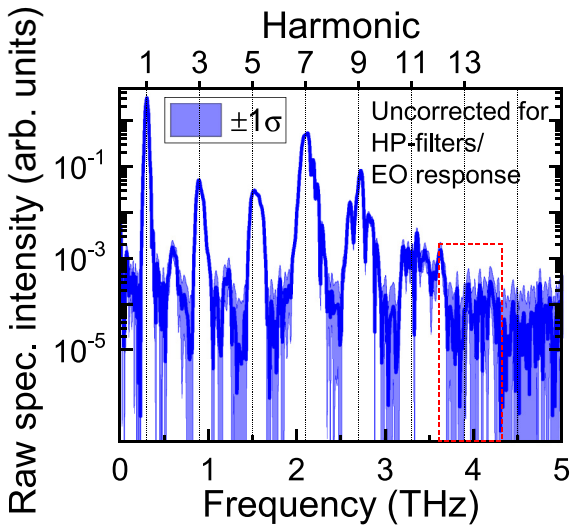

FIG. 22. Raw experimental spectrum ($T = 4$ K, Sample B, $N_d = 5.0 \times 10^{16}$ cm^{-3}, $L = 272$ μm, $E_0 = 81$ kV cm^{-1}) using additional high-pass filter to allow inspection of spectral region about the 13th harmonic (dashed rectangle), including $\pm 1\sigma$ confidence intervals.

absorption for the pump at high fields (main text, Fig. 3), we also reduce the Drude absorption α_1 using the experimental data to avoid an overestimate (i.e., by extrapolating the low-field linear dependence and calculating the bleach ratio). We show the estimates obtained for $\chi^{(n)}$ ($n = 3, 5, 7$) in Fig. 19, both based on the raw data, and after correcting for the Drude absorption and bleach effect.

8. Low-temperature HG: Time-domain fields and spectra

In Fig. 20 we plot the intensity spectra and filtered harmonics for the experiments at $T = 4$ K, obtained by applying a super-Gaussian filter $F_n(\nu) = \exp(-[(\nu - \nu_n)/\delta\nu]^\eta)$ with $\eta = 4$ and $\delta\nu = 100$ GHz. The corresponding filtered time-domain fields are shown in Fig. 21. In comparison to the results for $T = 300$ K (Figs. 15 and 16), one sees how the more complex spectral lineshapes result in more complex temporal envelopes, especially for $n = 7, 9$. For this reason, we use the emission fluence (as opposed to peak field) for the pump field dependence and comparison with MC-FDTD results in the main text (Fig. 6) for this case.

In Fig. 22 we also include an intensity spectrum (uncorrected for high-pass filters/EO-response) measured at $T = 4$ K including an additional high-pass filter, to allow a better resolution of harmonics with $n \geqslant 13$. As can be seen, a statistically significant signal level is indeed measured about the 13th harmonic (i.e., the lower confidence bound has not dropped fully to zero), albeit almost lost in the noise floor.

The pump-field-dependence experiments for $T = 300$ K and $T = 4$ K were performed on samples with different dopant concentration (to provide the best respective signal-to-noise), and hence their absolute HG yields cannot be compared directly [for T dependence with Sample A, see Fig. 5(e) in main text]. Nevertheless, for completeness, in Figs. 23(a) and 23(b) we present the respective results for the harmonic fluences vs pump field, with common scales.

9. Tunnel photoionization model

For the MC simulations at $T = 4$ K, we employed the literature models for the photoionization rate $w_{i,b}(E)$ ($b = \mathrm{hh}, \mathrm{lh}$) of the acceptor dopants, which are derived for a static field E [21,22], and applied here with the time-dependent pump field $E(t)$. This approach is at least valid in the strong-field regime [23–25], i.e., when $w_{i,b} \gg \nu_1$ (pump frequency ν_1), or equivalently $\gamma \ll 1$, where γ is the Keldysh parameter (see main paper). As stated in Ref. [22], the tunnel ionization process is dominated by light holes (the contribution from

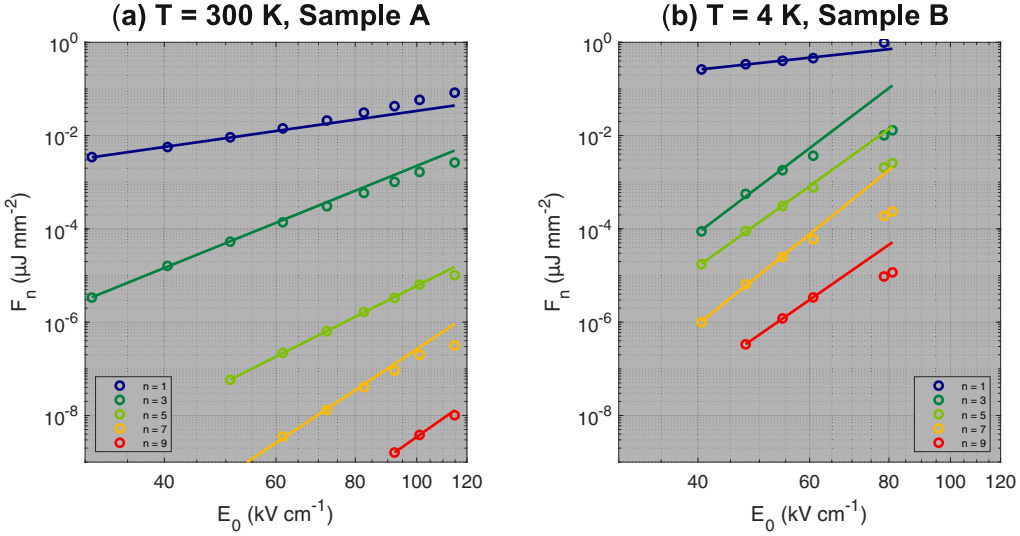

FIG. 23. Experimental emitted harmonic fluence vs peak pump field. (a) $T = 300$ K [Sample A: $N_d = 5.75 \times 10^{15}$ cm^{-3}, $L = 900$ μm, see also Fig. 17(b) above]. (b) $T = 4$ K [Sample B: $N_d = 5.0 \times 10^{16}$ cm^{-3}, $L = 272$ μm—only data for GaP EO detection, see also Fig. 6(a) in main paper].

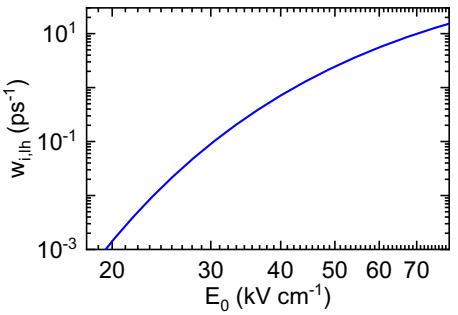

FIG. 24. Photoionization rate probability for light holes in Si:B, adopted from [22], used in the MC simulations for $T = 4$ K.

heavy holes emerging only at significantly higher fields [21]), and we take $w_{i,\mathrm{hh}} \to 0$ while for the light holes

$$w_{i,\mathrm{lh}} = w_0 \left(\frac{6\alpha}{E}\right)^{2n_{\mathrm{lh}}-1} \exp\left(-\frac{\alpha}{E}\right) \tag{A2}$$

where

$$w_0 = \frac{1}{\sigma^2[\Gamma(n_{\mathrm{lh}}+1)]^2}\frac{2I_p}{\hbar}, \quad \alpha = \frac{4\sqrt{2m_{\mathrm{lh}}}\cdot I_p^{3/2}}{3e\hbar},$$
$$n_{\mathrm{lh}} = \frac{e^2}{4\pi\epsilon\hbar}\sqrt{\frac{m_{\mathrm{lh}}}{2I_p}},$$

where $I_p = 45$ meV is the ionization energy, m_{lh} the light-hole mass, $\epsilon = \epsilon_0 \cdot \epsilon_r$ ($\epsilon_r = 11.8$) the background permittivity, and $\sigma^2 = 0.63$ [21]. This yields $n_{\mathrm{lh}} = 0.57$, $w_0 = 2.44 \times 10^{14}$ s^{-1}, and $\alpha = 250$ kV cm^{-1}. The corresponding ionisation rate is plotted in Fig. 24.

10. Photoionized hole recollision including scattering

The semiclassical model for the trajectories of photoionized charges [50], developed for the (low-density) gas phase, assumes the ballistic equation of motion $\partial_t v = qE(t)/m$, where $E(t)$ is the optical electric field (carrier frequency $\omega = 2\pi/T$) and one considers trajectories beginning at different intracycle times t_0 (the photoionization rate being highest at the field peaks, $t = \frac{1}{2}mT$). For a monochromatic field (amplitude E_0), this yields [with $x(t_0) = v(t_0) = 0$]

$$v(t > t_0) = \omega x_0[\sin(\omega t) - \sin(\omega t_0)],$$

and

$$x(t > t_0) = x_0\{[\cos(\omega t) - \cos(\omega t_0)] - \omega(t - t_0)\sin(\omega t_0)\}$$

where $x_0 = eE_0/m\omega^2$. For $t_0 \approx 0$, these trajectories return to the parent ion (at $x = 0$) at a time $t - t_0 \approx T$ (a full-field cycle later), while for $t_0 \to T/4$ this reduces to $t - t_0 \to 0$ ("short trajectories" [50]), although below saturation, very few charges are ionized away from $t_0 = 0$ (while for $-T/2 < t < 0$, the trajectories actually migrate from the parent ion and do not recollide).

In our case where rapid scattering takes place, one can consider an additional friction term for the equation of motion,

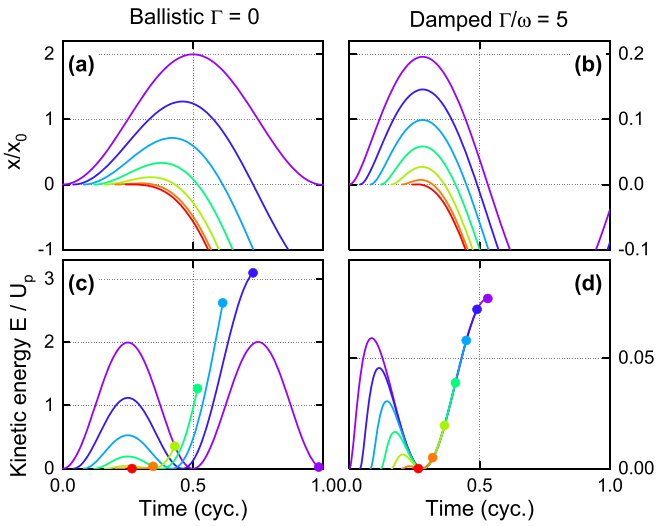

FIG. 25. Example [(a),(b)] trajectories and [(c),(d)] kinetic energy of photoionized charges vs time for (a) and (c) the ballistic case as assumed in dilute gas phase ($\Gamma = 0$) and (b) and (d) with intracycle scattering ($\Gamma/\omega = 5$) comparable to the solid-state situation for photoionized holes (note the different vertical scales). Each curve begins at its respective ionization time t_0. Kinetic energy curves terminated at recollision time.

$\partial_t v = qE(t)/m - \Gamma v$, albeit only an approximate description of the energy-dependent scattering rate in the MC simulations. One can solve this equation of motion to arrive at

$$v(t > t_0) = x_0 \frac{1}{1 + (\Gamma/\omega)^2}[Y(t) - e^{-\Gamma(t-t_0)}Y(t_0)],$$
$$Y(t) = \Gamma\cos(\omega t) + \omega\sin(\omega t),$$

and

$$x(t > t_0) = x_0 \frac{1}{1 + (\Gamma/\omega)^2} \times \left[\frac{Z(t) - Z(t_0)}{\omega} - \frac{Y(t_0)}{\Gamma}(1 - e^{-\Gamma(t-t_0)})\right],$$
$$Z(t) = \Gamma\sin(\omega t) - \omega\cos(\omega t),$$

as checked against numerical solutions to the equation of motion. Here, for $t \approx t_0$ and $\Gamma \gg \omega$, one finds that the Drude-like motion results in recollisions about $t - t_0 = T/2$, i.e., after only a *half*-cycle, as observed in the trajectories from MC simulations in the main text. Example trajectories are shown Fig. 25 for both the ballistic and damped cases for a set of $t_0 \in [0, T/4]$. Besides the earlier recollision time, ones also sees (i) the well-known maximum kinetic energy ($\mathcal{E}_{r,\max} = 3.17 \cdot U_p$ for an ionisation phase $\omega \cdot t_0 = 17°$) for the ballistic case [50], and (ii) the strongly reduced amplitude and kinetic energy for the damped case.

[1] F. Meng, F. Walla, Q. ul-Islam, A. Pashkin, H. Schneider, C. Jungemann, M. D. Thomson, and H. G. Roskos, Importance of valence-band anharmonicity and carrier distribution for third- and fifth-harmonic generation in Si:B pumped with intense terahertz pulses, Phys. Rev. B **106**, 075203 (2022).

[2] H. A. Hafez, S. Kovalev, J.-C. Deinert, Z. Mics, B. Green, N. Awari, M. Chen, S. Germanskiy, U. Lehnert, J. Teichert *et al.*, Extremely efficient terahertz high-harmonic generation in graphene by hot dirac fermions, Nature (London) **561**, 507 (2018).

[3] J.-C. Deinert, D. A. Iranzo, R. Pérez, X. Jia, H. A. Hafez, I. Ilyakov, N. Awari, M. Chen, M. Bawatna, A. N. Ponomaryov *et al.*, Grating-graphene metamaterial as a platform for terahertz nonlinear photonics, ACS Nano **15**, 1145 (2021).

[4] S. Kovalev, R. M. A. Dantas, S. Germanskiy, J.-C. Deinert, B. Green, I. Ilyakov, N. Awari, M. Chen, M. Bawatna, J. Ling *et al.*, Non-perturbative terahertz high-harmonic generation in the three-dimensional dirac semimetal Cd_3As_2, Nat. Commun. **11**, 2451 (2020).

[5] N. Dessmann, N. H. Le, V. Eless, S. Chick, K. Saeedi, A. Perez-Delgado, S. G. Pavlov, A. F. G. van der Meer, K. L. Litvinenko, I. Galbraith, N. V. Abrosimov *et al.*, Highly efficient THz four-wave mixing in doped silicon, Light Sci. Appl. **10**, 71 (2021).

[6] C. K. N. Patel, R. E. Slusher, and P. A. Fleury, Optical nonlinearities due to mobile carriers in semiconductors, Phys. Rev. Lett. **17**, 1011 (1966).

[7] A. Mayer and F. Keilmann, Far-infrared nonlinear optics. II. $\chi^{(3)}$ contributions from the dynamics of free carriers in semiconductors, Phys. Rev. B **33**, 6962 (1986).

[8] M. Urban, C. Nieswand, M. R. Siegrist, and F. Keilmann, Intensity dependence of the third-harmonic-generation efficiency for high-power far-infrared radiation in n-silicon, J. Appl. Phys. **77**, 981 (1995).

[9] C. C. Wang and N. W. Ressler, Nonlinear optical effects of conduction electrons in semiconductors, Phys. Rev. **188**, 1291 (1969).

[10] R. Brazis, R. Raguotis, and M. R. Siegrist, Suitability of drift nonlinearity in Si, GaAs, and InP for high-power frequency converters with a 1 THz radiation output, J. Appl. Phys. **84**, 3474 (1998).

[11] F. Meng, M. D. Thomson, Q. ul-Islam, B. Klug, A. Pashkin, H. Schneider, and H. G. Roskos, Intracavity third-harmonic generation in Si:B pumped by intense terahertz pulses, Phys. Rev. B **102**, 075205 (2020).

[12] A. Dargys and J. Kundrotas, *Handbook on the Physical Properties of Ge, Si, GaAs and InP*, Vol. 39 (Science and Encyclopedia Publishers, Lithuania, 1996)

[13] F. Langer, M. Hohenleutner, C. P. Schmid, C. Poellmann, P. Nagler, T. Korn, C. Schüller, M. S. Sherwin, U. Huttner, J. T. Steiner *et al.*, Lightwave-driven quasiparticle collisions on a subcycle timescale, Nature (London) **533**, 225 (2016).

[14] G. Lüpke, Characterization of semiconductor interfaces by second-harmonic generation, Surf. Sci. Rep. **35**, 75 (1999).

[15] C. Jungemann, S. Keith, M. Bartels, and B. Meinerzhagen, Efficient full band monte carlo hot carrier simulation for silicon devices, IEICE Trans. Electron. **E82-C**, 870 (1999).

[16] C. Jungemann and B. Meinerzhagen, *Hierarchical Device Simulation: The Monte-Carlo Perspective*, Computational Microelectronics (Springer, New York, 2003).

[17] C. Jungemann, F. Meng, M. D. Thomson, and H. G. Roskos, Massively parallel FDTD full-band Monte Carlo simulations of electromagnetic THz pulses in p-doped silicon at cryogenic temperatures, Solid-State Electron. **197**, 108439 (2022).

[18] C. Jungemann, M. Thomson, F. Meng, and H. Roskos, Massively parallel FDTD-FBMC simulations of nonlinear hole dynamics in silicon at cryogenic temperatures driven by intense em THz pulses, Solid-State Electron. **207**. 108683 (2023).

[19] N. H. Le, G. V. Lanskii, G. Aeppli, and B. N. Murdin, Giant non-linear susceptibility of hydrogenic donors in silicon and germanium, Light Sci. Appl. **8**, 64 (2019).

[20] M. Lewenstein, P. Balcou, M. Y. Ivanov, A. L'Huillier, and P. B. Corkum, Theory of high-harmonic generation by low-frequency laser fields, Phys. Rev. A **49**, 2117 (1994).

[21] A. Dargys and S. Žurauskas, Tunnel ionization of shallow acceptors and donors in GaAs, J. Phys.: Condens. Matter **7**, 2133 (1995).

[22] H. Q. Nie and D. Coon, Tunneling of holes from acceptor levels in an applied field, Solid-State Electron. **27**, 53 (1984).

[23] G. L. Yudin and M. Y. Ivanov, Nonadiabatic tunnel ionization: Looking inside a laser cycle, Phys. Rev. A **64**, 013409 (2001).

[24] H. R. Reiss, Limits on tunneling theories of strong-field ionization, Phys. Rev. Lett. **101**, 043002 (2008).

[25] N. Boroumand, A. Thorpe, A. M. Parks, and T. Brabec, Keldysh ionization theory of atoms: Mathematical details, J. Phys. B: At., Mol. Opt. Phys. **55**, 213001 (2022).

[26] S. D. Ganichev, A. P. Dmitriev, S. A. Emel'yanov, Y. V. Terent'ev, I. D. Yaroshetskii, and I. N. Yassievich, Impact ionization in semiconductors under the influence of the electric field of an optical wave, Sov. Phys. JETP **63**, 256 (1986).

[27] A. K. Ramdas and S. Rodriguez, Spectroscopy of the solid-state analogues of the hydrogen atom: Donors and acceptors in semiconductors, Rep. Prog. Phys. **44**, 1297 (1981).

[28] M. Lundstrom, *Fundamentals of Carrier Transport*, 2nd ed., digital version (Cambridge University Press, Cambridge, 2009).

[29] G. Vampa, C. R. McDonald, G. Orlando, D. D. Klug, P. B. Corkum, and T. Brabec, Theoretical analysis of high-harmonic generation in solids, Phys. Rev. Lett. **113**, 073901 (2014).

[30] G. Vampa, T. J. Hammond, N. Thiré, B. E. Schmidt, F. Légaré, C. R. McDonald, T. Brabec, and P. B. Corkum, Linking high harmonics from gases and solids, Nature (London) **522**, 462 (2015).

[31] H. Banks, B. Zaks, F. Yang, S. Mack, A. C. Gossard, R. Liu, and M. S. Sherwin, Terahertz electron-hole recollisions in GaAs/AlGaAs quantum wells: Robustness to scattering by optical phonons and thermal fluctuations, Phys. Rev. Lett. **111**, 267402 (2013).

[32] H. A. Hafez, S. Kovalev, K.-J. Tielrooij, M. Bonn, M. Gensch, and D. Turchinovich, Terahertz nonlinear optics of graphene: From saturable absorption to high-harmonics generation, Adv. Opt. Mater. **8**, 1900771 (2020).

[33] M. G. Kuzyk, J. Pérez-Moreno, and S. Shafei, Sum rules and scaling in nonlinear optics, Phys. Rep. **529**, 297 (2013).

[34] D. J. Passos, G. B. Ventura, J. M. B. L. dos Santos, and J. M. V. P. Lopes, Nonlinear optical conductivity of a two-band crystal I, J. Phys.: Condens. Matter **33**, 465701 (2021).

[35] S. Ghimire, A. D. DiChiara, E. Sistrunk, P. Agostini, L. F. DiMauro, and D. A. Reis, Observation of high-order harmonic generation in a bulk crystal, Nat. Phys. **7**, 138 (2011).

[36] Y. S. You, Y. Yin, Y. Wu, A. Chew, X. Ren, F. Zhuang, S. Gholam-Mirzaei, M. Chini, Z. Chang, and S. Ghimire, High-harmonic generation in amorphous solids, Nat. Commun. **8**, 724 (2017).

[37] Z. Wang, H. Park, Y. H. Lai, J. Xu, C. I. Blaga, F. Yang, P. Agostini, and L. F. DiMauro, The roles of photo-carrier doping and driving wavelength in high harmonic generation from a semiconductor, Nat. Commun. **8**, 1686 (2017).

[38] A. F. Kemper, B. Moritz, J. K. Freericks, and T. P. Devereaux, Theoretical description of high-order harmonic generation in solids, New J. Phys. **15**, 023003 (2013).

[39] H. Kitamura, Spherical-harmonics expansion method for density-matrix simulations of quantum electron dynamics in continuum states, Int. J. Quantum Chem. **115**, 1587 (2015).

[40] T. T. Luu and H. J. Wörner, High-order harmonic generation in solids: A unifying approach, Phys. Rev. B **94**, 115164 (2016).

[41] L. Yue and M. B. Gaarde, Imperfect recollisions in high-harmonic generation in solids, Phys. Rev. Lett. **124**, 153204 (2020).

[42] R. Buczko and F. Bassani, Shallow acceptor resonant states in Si and Ge, Phys. Rev. B **45**, 5838 (1992).

[43] E. E. Serebryannikov and A. M. Zheltikov, Strong-field photoionization as excited-state tunneling, Phys. Rev. Lett. **116**, 123901 (2016).

[44] Helmholtz-Zentrum Dresden Rossendorf, ELBE Center for High-Power Radiation Sources, JLSRF **2**, A39 (2016).

[45] G. Gallot and D. Grischkowsky, Electro-optic detection of terahertz radiation, J. Opt. Soc. Am. B **16**, 1204 (1999).

[46] S. Casalbuoni, H. Schlarb, B. Schmidt, P. Schmüser, B. Steffen, and A. Winter, Numerical studies on the electro-optic detection of femtosecond electron bunches, Phys. Rev. ST Accel. Beams **11**, 072802 (2008).

[47] E. D. Palik, *Handbook of Optical Constants of Solids*, Vol. 1 (Academic Press, New York, 1985).

[48] E. D. Palik, ed., *Handbook of Optical Constants of Solids II*, Vol. 2 (Academic Press, San Diego, 1991).

[49] D. Caughey and R. Thomas, Carrier mobilities in silicon empirically related to doping and field, Proc. IEEE **55**, 2192 (1967).

[50] P. B. Corkum, Plasma perspective on strong field multiphoton ionization, Phys. Rev. Lett. **71**, 1994 (1993).